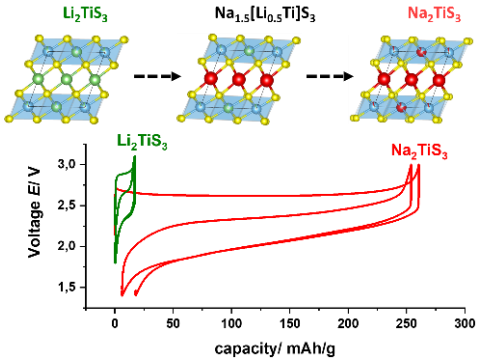
The layered sodium titanium trichalcogenide Na_2TiCh_3 framework (*Ch*= S, Se): A rich crystal and electrochemical chemistry.

Bernhard T. Leube[1,2], Elodie Salager[2,3], Erwan Chesneau[2,3], Gwenaëlle Rousse[1,2,4], Hervé Vezin[5], Artem M. Abakumov[6] and Jean-Marie Tarascon[1,2]

[1] Collège de France, Chaire de Chimie du Solide et de l'Energie, UMR 8260, 11 Place Marcelin Berthelot, 75231 CEDEX 05 Paris, France
[2] Réseau sur le Stockage Electrochimique de l'Energie (RS2E), FR CNRS 3459, 33 Rue Saint Leu, 80039 Amiens, France
[3]CNRS, CEMHTI, UPR3079, Université d'Orléans, 1D avenue de la recherche scientifique, Orléans, France
[4]Sorbonne Université, 4 Place Jussieu, F-75005 Paris, France
[5]Université Lille Nord de France, CNRS UMR8516, LASIRE, Villeneuve d'Ascq, France
[6]Center for Energy Science and Technology, Skolkovo Institute of Science and Technology, Nobel str. 3, 121205 Moscow, Russia

Abstract:



The synthesis and characterization of novel alkaline rich transition metal chalcogenides is an intriguing task for solid-state chemists and battery researchers. This class of materials allures by its rich compositional variety, high theoretical capacities and sometimes surprising electrochemistry. Using electrochemical inactive O3-type Li_2TiS_3 as a starting point, we embark on the synthesis and electrochemical characterization of five novel chalcogenides: Na_2TiS_3, Na_2TiSe_3, Na_2ZrS_3, Na_2ZrSe_3 and finally $Na_{1.5}[Li_{0.5}Ti]S_3$. All compounds crystallize in the layered O3 structure type, but show different electrochemical activity. In particular Na_2TiS_3 proves to be an interesting cathode material: the exchange of Li for Na unlocks electrochemical activity and allows for sustained electrochemical cycling of up to 1.8 Na per formula unit. We elucidate the structural evolution of the Na_xTiS_3 framework during cycling and find a reversible structural transformation from O3 to O1 stacking of the TiS_3 octahedral layers. These findings could help to understand the origin of anionic redox activity in the materials based on d^0 transition metals while opening another direction towards cathode materials comprising solely abundant elements.

Introduction

Li-ion batteries have emerged as the predominant solution for the storage of electric energy. However, new concepts of electroactive materials are needed to further push energy density, reduce costs and

improve safety and sustainability. As a viable substitute, Na-ion battery technology gains increased attention due to high abundance of sodium and perceived similarity to the highly developed Li-ion systems.

In analogy to O3-type (Delma's notation)[1] Li-rich layered oxides (*e.g.* Li_2IrO_3, Li_2RuO_3, Li_2MnO_3),[2–4] one could envisage the development of isostructural Na-rich cathode materials. However, only handful well characterized Na-rich O3-type oxides are known so far (Na_2RuO_3, Na_2ZrO_3, Na_2IrO_3)[5–7] - in particular stoichiometric 3*d* metal based materials are rare. The size mismatch between the NaO_6 and MO_6 octahedra coupled with a propensity of Na for prismatic coordination, favors crystallization of many compositions in the non-stoichiometric P2 structure type ($Na_xA_yTM_{1-x}O_2$ (A= alkaline metal, *TM*= transition metal; 0<x<1, y<1)). In search for sodium-rich phases, our group recently presented the mixed $Na_{1.5}Li_{0.5}IrO_3$ and $Na_{1.5}Li_{0.5}MnO_3$ O3-type phases, in which layers are formed by NaO_6 and mixed (Li/*TM*)O_6 octahedra. The strategy of partially substituting Li for Na alleviates the problems associated with the size mismatch in the mixed (A/*TM*)O_6 layer.[8,9]

Another angle towards sodium-rich materials is changing the ligand from O to the heavier chalcogenides S and Se, which can favor the formation of the O3-type structure. Colombet *et al.* reported crystalline Na_2TiS_3 in 1978 while investigating the Na_2S-TiS_2 system.[10] Based on visual inspection of the PXRD pattern, they speculated on structural similarity with Na_2SnS_3, implying a layered O3-type structure.[11] Pelé investigated Na_2TiS_3 for the first time as a cathode material (theoretical capacity of 282 mAh/g), but problems with the electrolyte (1M $NaPF_6$ in tetraethylene glycol dimethylether) prevented full exploitation of the theoretical capacity.[12] Following this lead, Nasu *et al.* described the synthesis and electrochemical cycling properties of three polymorphs of Na_2TiS_3: amorphous, cubic (disordered rock salt structure) and layered, which they targeted by applying different ball milling and heating procedures.[13,14] In all-solid-state cell configurations using glassy Na_3PS_4 as a solid electrolyte and $Na_{15}Sn_4$ as the anode, they achieved reversible capacities of 250 mAh/g (amorphous), 270 mAh/g (cubic) and 140 mAh/g (crystalline) in the voltage range of 0.8 V - 3.2 V.

Such high electrochemical activity in Na_2TiS_3 is somewhat surprising bearing in mind that Ti^{4+} has a d^0 electron configuration and that isostructural Li_2TiS_3 is electrochemically inactive. Thus, the answer must lie with the contribution of the anion sublattice to the charge compensation, implying $S^{2-/n-}$anionic redox. Sulfide-based materials exhibit a large range of formal oxidation states, ranging from S^{2-} in Li_2TiS_3, to mixed $S^{2-}/(S_2)^{2-}$ in TiS_3, to dimerized $(S_2)^{2-}$ in FeS_2 and finally to $(S_2)^{1-}$ in CuS_2.[15–19] This versatile anion redox chemistry was already exploited in Li_2TiS_3 by cation-doping (*e.g.* Ti^{3+}, Co^{2+}, Fe^{2+})[15,20,21] or ball milling,[22] which both unlock dynamic anionic redox processes upon electrochemical cycling. Recently, we substituted S^{2-} for Se^{2-} along the full $Li_2TiS_{3-x}Se_x$ solid solution and observed a bell shaped activation curve, *i.e.* the endmembers exhibit negligible activity while the mixed compounds show significant capacity. We proposed that introduction of Se breaks the local symmetry and leads to local distortions around the Ti*Ch*$_6$ (*Ch*= S, Se) octahedra, which activates anionic redox.[23] Intrigued by this novel approach to anionic redox in d^0 *TM* based materials, we decided to revisit Na_2TiS_3, its structural homologues Na_2TiSe_3, Na_2ZrS_3, Na_2ZrSe_3 and finally the mixed $Na_{1.5}[Li_{0.5}Ti]S_3$ phase in an attempt to strengthen our understanding of anionic redox in sulfide based materials.

In a first step, we examined the synthetic conditions for crystalline Na_2MCh_3 (*M*= Ti, Zr; *Ch*= S, Se). As reported, one can readily obtain a crystalline Na_2TiS_3 phase by sintering the binaries Na_2S and TiS_2 in evacuated quartz tubes at 773 K, while the firing conditions were optimized for the other compositions (see SI). Crystalline Na_2TiS_3 demonstrates electron diffraction patterns (ED) characteristic of a layered O3-type structure (Figure 1a) manifested by the sharp brightest spots which can be indexed with the $R\bar{3}m$ unit cell (*a*= 3.7 Å, *c*= 19.7 Å). EDX compositional maps (Figure S1) of the Na_2TiS_3 sample indicate

homogeneous distribution of Na, Ti and S. Quantitative analysis gives a Na:Ti:S atomic ratio of 2.02(4):0.97(4):3.01(3), which is in good agreement with the nominal composition. Robust "honeycomb" ordering of the Na and Ti cations in the mixed $[Na_{1/3}Ti_{2/3}]$ layers is indicated by extra spots and diffuse intensity lines along **c*** clearly visible in the [-110] ED pattern. The interlayer ordering is however violated by numerous stacking faults visible in the [110] HAADF-STEM image (Figure 1b). The "honeycomb" superstructure can be more rigorously described by a monoclinic distortion of the rhombohedral cell. A combined SXRD/NPD[24] Rietveld refinement was carried out in the monoclinic space group $C2/m$ (Figure S2, Table S1) which confirms that Na_2TiS_3 adopts an O3-type structure, in which edge-sharing MS_6 octahedra (*M*= Na, Ti) form two types of layers: $[Na]S_2$ layers and partially honeycomb ordered $[Na_{1/3}Ti_{2/3}]S_2$ layers, which are stacked along the *c* axis. Minor traces of TiO_2 (Anatase, Rutile) were detected in the SXRD pattern which originate from oxide impurities in the commercial Na_2S precursor. Rietveld refinements of the heavier homologues (Figure S3, S4, Table S2-S4), show that Na_2TiSe_3, Na_2ZrS_3 and Na_2ZrSe_3 crystallize isostructurally to Na_2TiS_3, in accordance with what had already been reported for the zirconates.[25,26] In the case of Na_2ZrS_3, additional superstructure reflections associated with O6 stacking sequences are clearly visible (inset Figure S4a). The origin of these has already been thoroughly discussed for $Na_3Ni_2BiO_6$[27] and $Na_{1.5}[Li_{0.5}Ir]O_3$.[8]

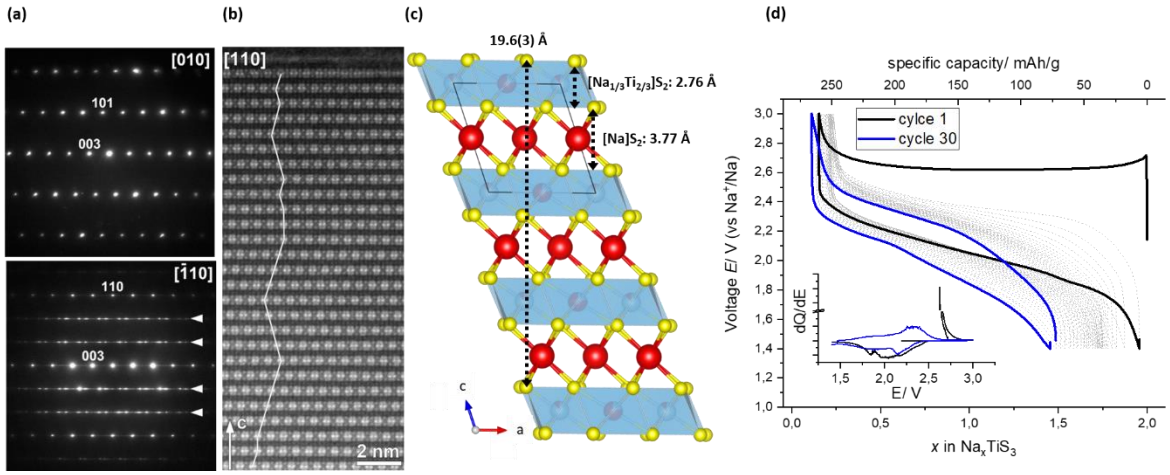


Figure 1: Structural and electrochemical characterization of Na_2TiS_3 (a) ED patterns indexed with the $R\bar{3}m$ space group, reflections and diffuse intensity due to the Na-Ti "honeycomb" ordering are marked with arrowheads. (b) [110] HAADF-STEM image, stacking faults along c are visible by random lateral displacements of the $[Na_{1/3}Ti_{2/3}]S_2$ blocks traced with zig-zag line. (c) structural model as obtained from a combined SXRD-NPD Rietveld refinement viewed along the b axis, forming a layered O3-type structure. (d) Galvanostatic cycling of Na_2TiS_3 vs Na^+/Na. Atoms and polyhedral are colored as follows - red: sodium; blue: titanium; sulfur: yellow.

In 2020 Saha proposed the use of 1 M $NaPF_6$ in propylene carbonate (PC) as electrolyte in a Na_2TiS_3|Na electrochemical cell, which improved the reversibility of the cycling.[28] Galvanostatic experiments on Na_2MCh_3 (*M*= Ti, Zr; *Ch*= S, Se) *vs* Na^+/Na confirm the suitability of this electrolyte, as up to 1.8 Na can be extracted on oxidation from the titanates (Figure 1d). In the case of Na_2TiS_3, close inspection of the voltage trace reveals a bump at the onset of the initial oxidation, which is not present for Na_2TiSe_3 (Figure S3b). This potential spike is followed by a plateau indicative of a biphasic process. On subsequent cycling, the voltage trace changes to an S-shape, symptomatic of the formation of solid-solutions between the charged and discharged states. The average voltage is lowered on going from the sulfide to the selenide which is a direct consequence from the lower electronegativity of Se compared to S, similar to observed in $Li_2TiS_{3-x}Se_x$ or $Li_2FeS_{2-x}Se_x$.[23,29] Throughout cycling both materials are plagued by voltage hysteresis, but better orbital overlap in the selenides allows for a partial reduction of the voltage gap in Na_2TiSe_3 to 240 mV as compared to 500 mV in the Na_2TiS_3. This extremely high polarization can be lowered to 250 mV in a GITT experiment after a 4 h relaxation

period (Figure S5a). Upon 30 cycles the capacity drops drastically by 25 % and 65% in Na_2TiS_3 and Na_2TiSe_3, respectively, coupled to significant voltage fade. To verify that the electrochemical capacity in Na_2TiS_3 is not simply triggered by an off-stoichiometric pristine material (presence of Ti^{3+}), we started electrochemical cells on discharge. However, the first discharge capacity is negligible (Figure S5b). Interestingly, opening the discharge voltage to 0.2 V does not lead to the reversible utilization of the Ti^{4+}/Ti^{3+} couple, which in TiS_2 is responsible for the electrochemical activity. At the precise stoichiometry of Na_2TiS_3, all octahedral voids are occupied, leaving only tetrahedral interstices for hosting additional Na^+ ions. Instead of intercalation, the voltage curve indicates conversion type reaction at low potentials leading to irreversible structural degradation (Figure S5c). Turning to the zirconates, these materials exhibit nearly no reversible capacity at all. Introduction of more electropositive Zr raises energy of the empty cationic d-bands and consequently increases the band gap, which is corroborated by a color change from black/grey (Na_2TiS_3) to brown/orange (Na_2ZrS_3). Eventually this increased band gap reduces electronic conductivity of Na_2ZrS_3 and thus impedes bulk oxidation.

To gain more insight into this structural transformation, we carried out *operando* PXRD and *ex situ* SXRD experiments on Na_2TiS_3 and Na_2TiSe_3 cycled *vs* Na^+/Na. In both materials, the first oxidation process is of biphasic nature: a broad reflection associated with the formation of a secondary Na_xTiCh_3 phase grows gradually in intensity, while the pristine material is consumed (Figure 2a, Figure S3c). At full charge Na_xTiCh_3 exhibits low crystallinity – only the 00*l* reflection, associated with the interlayer spacing is well defined (*d*= 6 Å) (SXRD pattern, Figure 2b), impeding meaningful structural refinement. Upon discharge a solid-solution is formed with concomitant increase of crystallinity. The discharged Na_2TiS_3 material regains its O3-type structure, as determined by a Rietveld refinement on SXRD data (Figure 2c,d; Table S5). However, the Na-Ti honeycomb ordering is lost and notable peak broadening coupled to increased isotropic atomic displacement parameters U_{iso} reflect a considerable degree of disorder. On consecutive cycling, a reversible solid-solution is formed along Na_2TiCh_3-Na_xTiCh_3. This response to oxidation contrasts starkly with Li_2TiS_3, which is electrochemically inactive and with the structural evolution of $Li_2TiS_{2.4}Se_{0.6}$, for which a monophasic response upon oxidation was witnessed.

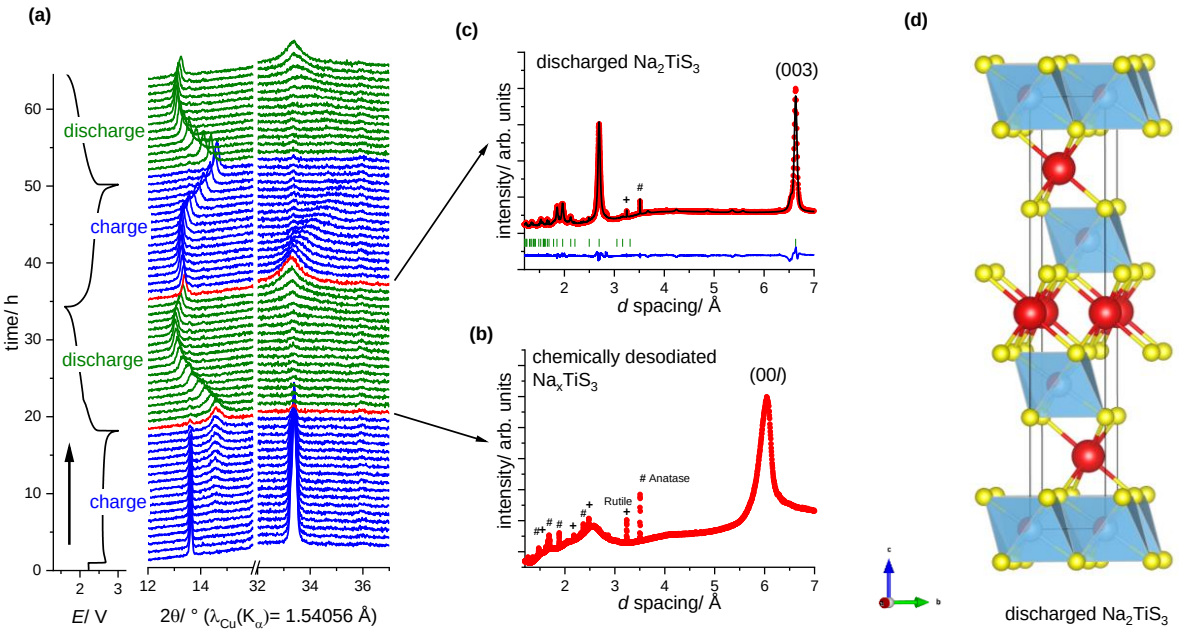


Figure 2: Structural evolution of Na_2TiS_3 cycled against Na^+/Na (a) operando PXRD experiment on two electrochemical cycles (b) SXRD pattern of chemically charged Na_xTiS_3, the symbols '#' and '+' denote the position of the Bragg reflections of the electrochemically inactive TiO_2 polymorphs Rutile and Anatase, already observed in the pristine material. The charged Na_xTiS_3 material is manifested by a broad reflection at d= 6 Å. (c) Rietveld refinement of discharged Na_2TiS_3 based on SXRD data (d) Refined structural model of discharged Na_2TiS_3. Atoms and polyhedral are colored as follows - red: sodium; blue: titanium; sulfur: yellow.

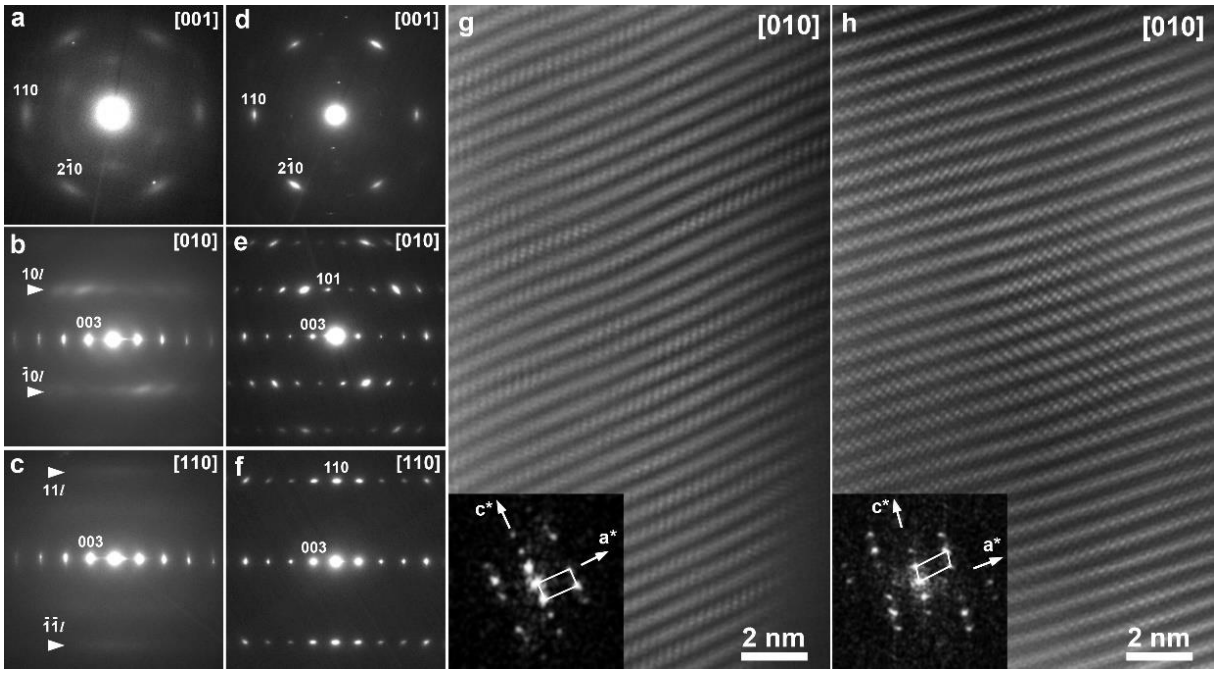


Figure 3: Structural evolution of Na_2TiS_3 upon desodiation (a,b,c,g) and subsequent sodiation (d,e,f,h). The ED patterns are indexed with the $R\bar{3}m$ space group. The h0l and hhl diffuse intensity lines in the ED patterns of the desodiated phase (a,b,c) are marked with arrowheads. Fourier transforms are shown as insets in the HAADF-STEM images of the desodiated (g) and sodiated (h) phases; the reciprocal lattice mesh is outlined in the Fourier transforms.

The structure changes upon desodiation and sodiation of Na_2TiS_3 were finally assessed with transmission electron microscopy. The ED patterns of the desodiated phase (Figure 3a,b,c) demonstrate only the 00*l* reflections which remain relatively sharp whereas all other reflections are substituted with poorly structured diffuse intensity manifesting itself as elongated blobs in the [001] ED pattern and as broad lines of modulated intensity in the [010] and [110] ED patterns. This picture is very typical for the layered systems with 2D disorder in which the layers remain regularly spaced causing sharp 00*l* reflections whereas the atomic positions within the layers and between the layers lose coherency. In fact, elongation of the 00*l* reflections in the direction perpendicular to **c*** (Figure 3b,c) also indicates that the layers demonstrate small local variation of orientation (*i.e*. become wavy). These features are supported by [010] HAADF-STEM image (Figure 3g) which shows that the layers contain ordered and disordered areas. The latter are visible by absence of clear dot pattern which becomes smeared due to loss of electron channeling conditions caused by random atomic displacements. Fourier transform from the locally ordered area indicates changing of the layer stacking mode from O3 to O1 (seen by a rectangular reciprocal lattice mesh outlined in the Fourier transform (insert in Figure 3g). Local disorder and gliding of the layers introduce strong strain causing wave-like deformation of the layers, also easily discernible from Figure 3g. Upon sodiation the atomic order within the layers is largely restored as is evident from sharpening of the reflections in the ED patterns (Figure 3d,e,f) and clear pattern of atomic columns in the [010] HAADF-STEM image (Figure 3h). The [010] ED pattern (Figure 3e) and Fourier transform of the HAADF-STEM image (see the oblique reciprocal lattice mesh in the insert in Figure 3h) show that the O3 stacking is fully recovered. Absence of "honeycomb" reflections (compare the [-110] ED patterns in Figure 1a and Figure 3f) witnesses

complete suppression of the Na-Ti intralayer ordering. Shuffling the Ti atoms upon suppression of the "honeycomb" ordering might be at the origin of strong local atomic disorder observed in the desodiated phase.

Motivated by these results we assembled Na_2TiS_3|Li cells (electrolyte: LP30). Interestingly, these cells show very similar electrochemical behavior, even though we evidence a significantly smaller polarization (Figure S6) compared to cycling *vs* Na. The voltage gap is reduced to 350 mV at C/10 rate and can be mitigated to 170 mV in a GITT experiment after 4 h relaxation. *Operando* PXRD experiments in the Na_2TiS_3|Li configuration show that the material follows the same structural path as when cycled *vs* Na, in particular forming a very disordered A_xTiS_3 (*A*= Li, Na; x< 0.3) framework at the end of charge. Already in the 1980's, crystalline TiS_3 (obtained by calcination of Ti and S at 773 K) was identified as a potential high-energy cathode material due to its large theoretical capacity. Up to three Li ions can be inserted utilizing both the anionic $(S_2)^{2-}/S^{2-}$ and cationic Ti^{4+}/Ti^{3+} redox couples. But at that time the application of TiS_3 was hampered by limited reversibility and voltage fade.[30–34] Intrigued, we directly synthesized electrochemically active A_xTiS_3 via two routes: (a) electrochemical desodiation of Na_2TiS_3 (b) chemical desodiation of Na_2TiS_3 using I_2 in acetonitrile. Both materials demonstrate reversible discharge capacities (>275 mAh/g) and high energy densities (> 600 Wh/kg) when cycled against a Li anode (Figure 4).

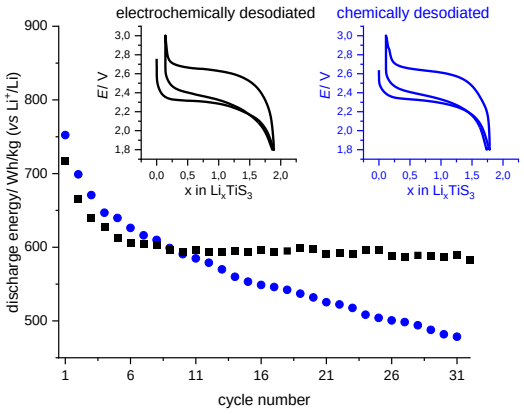


Figure 4: Electrochemical behavior of desodiated Na_xTiS_3 (x < 0.3) cycled against a Li metal anode.

In $Li_2TiS_{3-x}Se_x$, we previously identified local distortions of the heteroleptic Ti*Ch*$_6$ octahedra as the key to unlock anionic redox.[23] In order to get a grasp on local distortion in Na_2TiS_3 compared to Li_2TiS_3, EPR experiments were run at ambient temperature, 110 K and 5 K (Figure 5a, Figure S7). While the spectra for Li_2TiS_3 are featureless at ambient temperature except for a signal of a non-localized electron (g= 2.0024), we notice a more complicated spectrum for Na_2TiS_3. In addition to a signal of the free electron, we observe an anisotropic Ti^{3+} environment with three distinct g values (g_x= 1.985, g_y= 1.962, g_z= 1.946). The onset of a Ti^{3+} signal, not expected at first in $Na_2Ti^{4+}S_3$, was previously explained for $Li_2TiS_{3-x}Se_x$ from an internal ligand-to-metal charge transfer by temperature-driven electron localization.[23] With decreasing temperature, one can follow increased distortion of the octahedral symmetry with finally a fully localized electron on the Ti orbital at 5 K in both compounds (Figure 5b). While in Li_2TiS_3 dipolar interactions between Li and Ti dominate, echo detection mode uncovers superhyperfine coupling in Na_2TiS_3. The pseudo modulation of the spectrum (inset) shows two sets of 7 lines for the two eigenvalues (g_x, g_y) of the Ti^{3+} tensor. These lines can be attributed to Fermi contact coupling of Ti^{3+} with two equivalent sodium nuclei (I= 3/2). Thus, the temperature dependent distortion of the TiS_6 octahedra is accompanied by a shortening of the Na-Ti distance.

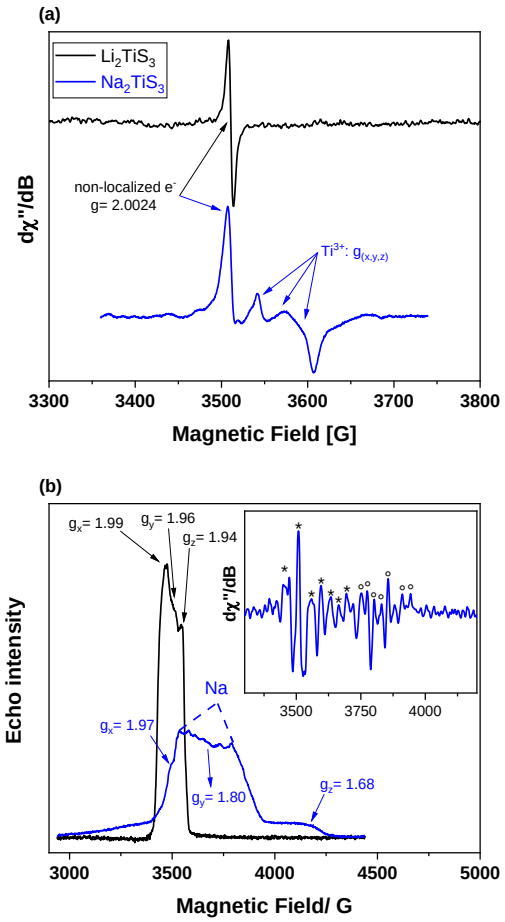


Figure 5: EPR spectra of Li_2TiS_3 (black) and Na_2TiS_3 (blue) at (a) ambient temperature and (b) at 5 K. The inset shows the superhyperfine coupling between g_x and g_y of the anisotropic Ti^{3+} with two equivalent Na atoms (nuclear spin I=3/2), which results in 2nI+1 liner per coupling (in total 2x7 lines).

Analysis of interatomic distances and bond lengths of the crystallographic models obtained by Rietveld refinement show that the "cubic" close-packed anion sublattice is significantly distorted in Na_2TiS_3 compared to Li_2TiS_3. By comparing the 12 closest S-S contacts for the crystallographically distinct S1 and S2 atoms in both materials, we clearly see a wider spread of the distances in Na_2TiS_3 (3.2 Å - 4.5 Å) in contrast to Li_2TiS_3 (3.3 Å - 3.9 Å) (Figure 6a). This is equivalently expressed by more irregular bond lengths in the SM_6 octahedra (M= Li, Na, Ti) (Figure 6b). Interestingly, the Ti1-S and Ti2-S bond lengths are very uniform (Figure 6c). Similarly, we cannot identify a significant difference in distortion of the AS_6 octahedra between Na_2TiS_3 and Li_2TiS_3 (Figure 6d). In conclusion, we state that the MS_6 metal octahedra are not significantly distorted, but that a distortion of the anion sublattice in Na_2TiS_3 is caused by the significantly longer intralayer distance in the $[Na]S_2$ slab (3.77 Å) compared to the mixed $[Na_{1/3}Ti_{2/3}]S_2$ slab (2.76 Å) (see Figure 1), which are more even in Li_2TiS_3. A similar conclusion can be reached when analyzing the crystallographic model of Na_2TiSe_3 (Figure S8).

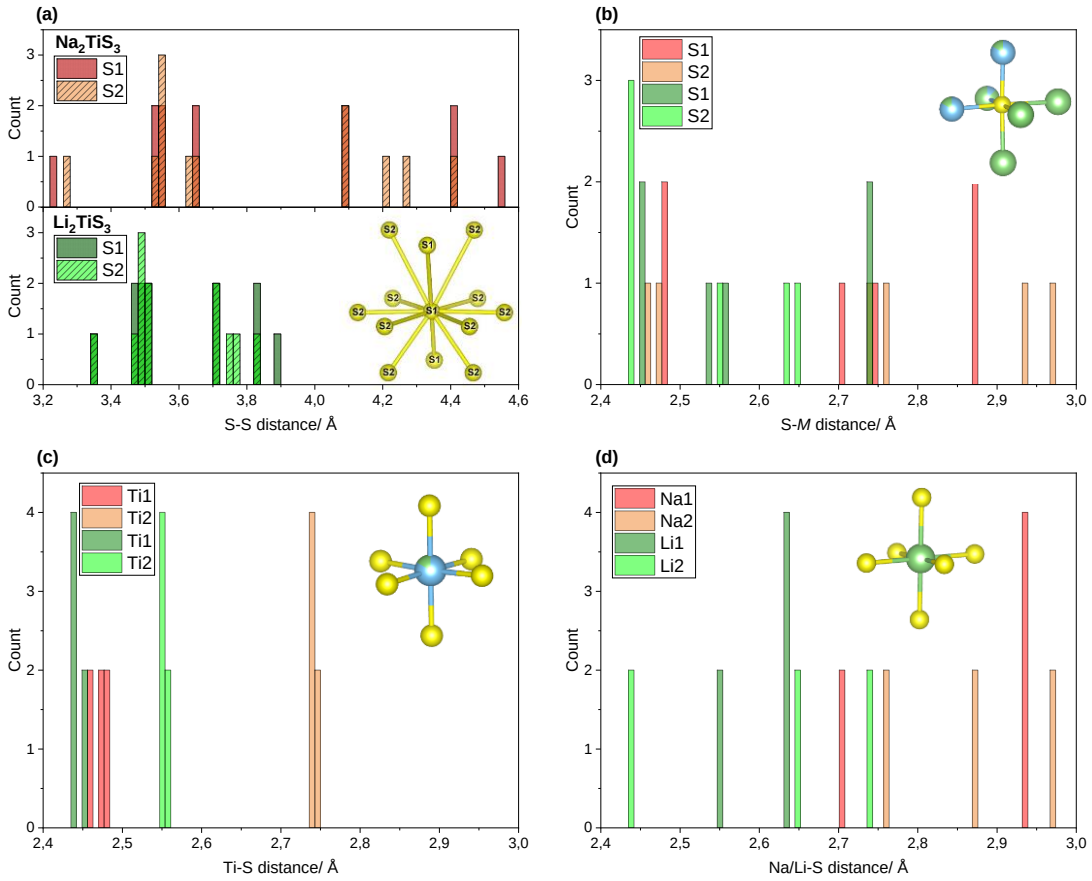


Figure 6: Analysis of atomic distances in Na_2TiS_3 and in Li_2TiS_3 based on the crystallographic models. (a) distance between a given sulphur atom (S1 or S2) in the cubic close packed anion sublattice and its 12 nearest neighbors respectively. (b) bond lengths in a given SM_6 octahedron. (c) bond lengths in a given TiS_6 octahedron. (d) bond lengths in a given AS_6 octahedron (A= Li, Na). Color code: red: Na_2TiS_3, green: Li_2TiS_3. Atoms are colored as follows - sulfur: yellow; blue : titanium; green: Li/Na.

$Na_{1.5}[Li_{0.5}Ti]S_3$

To complete the investigation of this interesting class of materials, we explore the mixed alkaline Na_2TiS_3-Li_2TiS_3 (=$Na_{2-x}Li_xTiS_3$) tie-line. The PXRD patterns of the *x*= 0, 0.5, 1.0, 1.5, 2 samples synthesized at 773 K are shown in Figure 7.

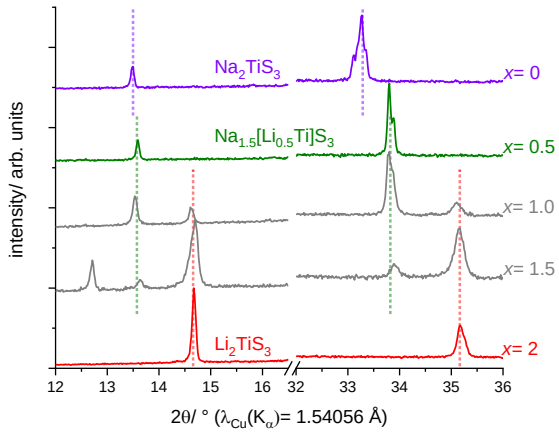


Figure 7: PXRD patterns of the reaction products obtained during the synthesis of the $Na_{2-x}Li_xTiS_3$ compositions. The vertical lines indicate the position of the expected Bragg reflections for Li_2TiS_3 (red), Na_2TiS_3 (purple) and the new $Na_{1.5}[Li_{0.5}Ti]S_3$ phase (green).

Alike for the $Na_{2-x}Li_xMnO_3$, we do not observe the formation of a solid solution, as for *x*= 1.5 and *x*= 1.0 multiple phases form. However, the composition of *x*= 0.5 ($Na_{1.5}Li_{0.5}TiS_3$) yields a single-phase PXRD pattern reminiscent of an O3-type structure. EDX analysis of the as-synthesized $Na_{1.5}Li_{0.5}TiS_3$ gives a Na:Ti:S ratio of 1.48(7):1.04(5):3.00(4) for the main phase, which corresponds nicely with the nominal composition. Given that $Na_{1.5}Li_{0.5}TiS_3$ is a stoichiometry-precise compound, we investigated the alkaline cation distribution among the layers by combined Rietveld refinement using NPD and SXRD data and TEM experiments. The best Rietveld fit could be obtained by entirely segregating Li and Na resulting in fully occupied $[Na]S_2$ and honeycomb ordered $[Li_{1/3}Ti_{2/3}]S_2$ layers with negligible degree of alkaline metal intermixing (Figure S9, S10, Table S6). Comparing the intensity profiles along the cationic columns in the [010] and [110] HAADF-STEM images of $Na_{1.5}Li_{0.5}TiS_3$ and Na_2TiS_3 confirms this assumption: virtually no intensity is detected at the Li sites of the $[Li_{1/3}Ti_{2/3}]S_2$ layers, whereas noticeable intensity is seen at the Na sites in $[Na_{1/3}Ti_{2/3}]S_2$ (Figure S11, S12). Both SXRD and TEM experiments reveal the presence of trace amounts of titanium dioxide (Anatase, Rutile), Na_2TiS_3 and $Na_5Li_3Ti_2S_8$ (compare to Table S7).[35]

The exchange of Na for Li in Na_2TiS_3 has a notable impact on the electrochemical behavior: while from Na_2TiS_3 up to 1.8 alkaline cations can be extracted upon oxidation, we succeed on the removal of solely 1.5 alkaline cations from $Na_{1.5}[Li_{0.5}Ti]S_3$ (regardless of whether cycled *vs* Na^+/Na or Li^+/Li) (Figure S13). This threshold links well the stoichiometry with the layered structure motif. Thus, we speculate that upon oxidation predominantly Na atoms are removed from the material, while the Li atoms remain inert – similar to observed in $Na_1[Li_{1/3}Mn_{2/3}]O_2$ and $Na_{0.75}[Li_{0.25}Mn_{0.75}]O_2$.[9,36] Furthermore, the voltage traces differ significantly when cycled against sodium or lithium anodes: an increased polarization persists during subsequent cycles when cycled *vs* Na^+/Na, while the cycling *vs* Li^+/Li mirrors the behavior of Na_2TiS_3. GITT experiments during the 2nd electrochemical cycle reveal that this hysteresis is attributed to kinetic effects, as the relaxed voltage traces of $Na_{1.5}[Li_{0.5}Ti]S_3$ cycled *vs* Na^+/Na or Li^+/Li match closely. Interestingly the average discharge voltage of Na_2TiS_3 and $Na_{1.5}[Li_{0.5}Ti]S_3$ cycled against Li^+/Li are very close. Lastly, *operando* PXRD experiments of cells cycles against Na^+/Na and Li^+/Li reveal that $Na_{1.5}[Li_{0.5}Ti]S_3$ undergoes the same structural process upon electrochemical cycling as Na_2TiS_3.

Finally, an NMR study was carried out on Na_2TiS_3 and $Na_{1.5}[Li_{0.5}Ti]S_3$ at different states of charge, as this technique allows for the study of the local order in low-crystalline materials and the quantification of the Li and Na content. Figure 8 shows the experimental and predicted ^{23}Na and ^{7}Li spectra of Na_2TiS_3 and $Na_{1.5}[Li_{0.5}Ti]S_3$ at different states of charge.

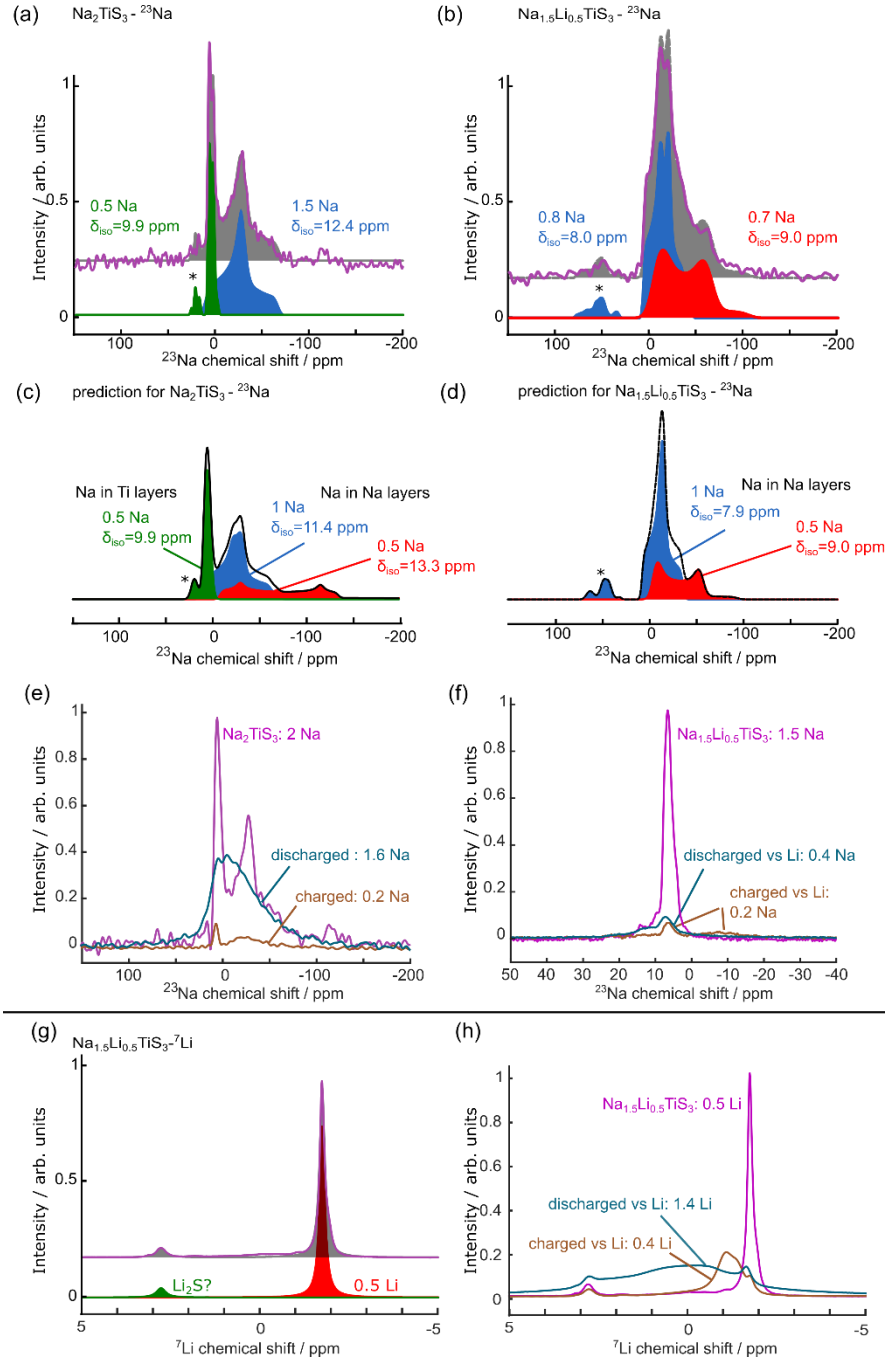


Figure 8: ^{23}Na solid-state NMR spectra and fits of (a) Na_2TiS_3 and (b) $Na_{1.5}[Li_{0.5}Ti]S_3$. The Na content is obtained by the integration of the components of the fit. The asterisk indicates the band n=0 of the satellite transition. (c, d) Predicted ^{23}Na spectra based on the crystallographic models. (e, f) Quantitative analysis of the ^{23}Na NMR spectra upon charge and discharge. (g) Experimental ^{7}Li NMR spectrum and fit of $Na_{1.5}[Li_{0.5}Ti]S_3$. An impurity phase is detected at 2.8 ppm which might relate to Li_2S. (h) Quantitative analysis of the ^{7}Li NMR spectra upon charge and discharge vs Li^+/Li.

The ^{23}Na NMR spectrum for Na_2TiS_3 (Figure 8a) reveals a broad signal accounting for 1.5 Na (blue) and a sharper signal corresponding to 0.5 Na (green), which we relate to the different Na environments in the $[Na]S_2$ and the mixed $[Na_{1/3}Ti_{2/3}]S_2$ layers respectively. The complex shapes of the signals are due to the quadrupolar nature of the Na atomic spins (see SI, Tables S8-S11). In contrast the ^{23}Na NMR spectrum of $Na_{1.5}[Li_{0.5}Ti]S_3$ (Figure 8b) is characterized by two broad signals accounting for 0.8 and 0.7 Na, indicative of non-symmetric environments. In order to confirm the negligible cation interlayer mixing, we performed planewave GIPAW predictions of the shifts based on the crystal structures. This approach was validated for Na_2TiS_3 (Figure 8c): the assignment is confirmed with a sharp (green) signal

for Na in $[Na_{1/3}Ti_{2/3}]S_2$ layers and two broad signals (blue and red) for Na in the $[Na]S_2$ layer. Na mobility in that $[Na]S_2$ layer results in the average signal detected experimentally. We then calculated the shifts for the mixed compound $Na_{1.5}[Li_{0.5}Ti]S_3$ for the structure containing negligible cation interlayer mixing and obtained a good agreement (Figure 8d). When charged, the ^{23}Na signal almost completely disappears for both materials, while the ^{7}Li signal of the mixed phase is only slightly lowered. The charged samples have nominal compositions of $Na_{0.2}TiS_3$ (Figure 8e) and $Na_{0.2}[Li_{0.4}Ti]S_3$ respectively (Figure 8f,h). The significant broadening of the ^{7}Li peak could be due to disorder induced by the amorphisation and/or Li migration, but we clearly observe a preferred removal of Na compared to Li. Upon discharge, a broad ^{23}Na signal reappears for Na_2TiS_3 indicating the reinsertion of 1.4 Na. Discharge against Li^+/Li results in preferential Li insertion with the resulting composition $Na_{0.4}Li_{1.4}TiS_3$. Quantitative analysis of the Na and Li content in the material confirms a combined alkaline metal content of $A_{1.9}TiS_3$ as obtained from coulombic titration.

Discussion/conclusion

The layered A_2TiCh_3 family proves to be a versatile framework for fine-tuning structural and electrochemical properties. By moving from Li_2TiS_3 to Na_2TiS_3 and finally to Na_2TiSe_3, we detect reversible electrochemical activity in the $TiCh_3$ framework. Desodiation of Na_2TiS_3 yields a metastable Na_xTiS_3 polymorph, which shows high discharge energy when cycled against a Li electrode (600 Wh/kg). Due to the d^0 electron configuration in Ti^{4+} we associate this capacity to redox processes on the anion framework, although the underlying mechanisms have not been fully understood so far. Preliminary DFT calculations show that the band gap in Na_2TiS_3 is larger than in Li_2TiS_3, thus ruling out that increased electronic conductivity is responsible for electrochemical activation in Na_2TiS_3. Analysis of EPR spectra and the crystallographic models indicate increased distortion of the S sublattice in Na_2TiS_3 compared to Li_2TiS_3. However, these observations must be more rigorously tied to the emergence of electrochemical activity in A_2TiCh_3 phases and consequently put into context of structural prerequisites for anionic redox. An in-depth computational paper dedicated to the charge compensation mechanisms in this family of materials is in preparation. Nevertheless, another explanation could lie in the energetics of the reaction pathway of the alkaline metal-driven electrochemical transformation from the pristine A_2TiS_3 to the activated TiS_3 framework. Introduction of more polarizable Se or Na might induce lattice softening and result in increased structural flexibility of the $TiCh_3$ framework. Consequently, structural transformations in Na_2TiS_3 (O3 – O1) or $Li_2TiS_{3-x}Se_x$ (O3 – O3) might be possible due to lower kinetic barriers, while being impeded in Li_2TiS_3.

Along the Li_2TiS_3-Na_2TiS_3 tie-line we find only one stable compound, O3-type $Na_{1.5}[Li_{0.5}Ti]S_3$. NMR studies at different states of charge reveal that Na is preferentially removed from $Na_{1.5}[Li_{0.5}Ti]S_3$. As already observed in $Na_{1.5}[Li_{0.5}M]O_3$ (M= Mn, Ru), the precise Na:Li ratio is governed by the formation of distinct $[Na]S_2$ and mixed $[Li_{1/3}Ti_{2/3}]S_2$ layers. We finally test this rational of mixing alkaline metals to stabilize the O3 structure motif by applying it to the A_2TiO_3 (A= Li, Na) system. In contrast to O3-type Li_2TiO_3,[37] Na_2TiO_3 is known to crystallize in three different non-layered polymorphs.[38] We hypothesize that mixing of Na and Ti in hypothetical $[Na_{1/3}Ti_{2/3}]O_3$ layers incurs an energetic penalty but that this could be alleviated by synthesizing a mixed $Na_{1.5}[Li_{0.5}Ti]O_3$ compound. $Na_{1.5}[Li_{0.5}Ti]O_3$ was consequently targeted by calcination of Na_2CO_3, Li_2CO_3 and TiO_2 (Anatase) at 923 K for 12 h. Indeed, analysis of the reaction product reveals the formation of an O3-type structure, as the main reflections of the PXRD pattern can be indexed to the rhombohedral $R\bar{3}m$ space group (a= 3.00201(7) Å, c= 16.0751(6) Å) (Figure S14). Additional superstructure reflections and a Li_2TiO_3 impurity are present at 4 Å < d < 5 Å. Upon oxidation the material exhibits a short plateau at 4.6V vs Li^+/Li in the first cycle at which ~0.3 A can be removed. However, almost no capacity is recovered on discharge. In transition metal oxides,

such an irreversible oxidation process ('activation plateau') is commonly associated to oxygen evolution.

We conclude that the layered transition metal chalcogenides (A_2Ti*Ch*) constitute an exciting and challenging field for solid-state chemists in the search for new materials. The compositional diversity enables rational tailoring of electrochemical properties while allowing for the study of elusive phenomena such as anionic redox. We presented a strategy to unlock the electrochemical activity in the TiS_3 framework, nurturing the long sought after dream of developing high-energy cathode materials devoid of expensive, rare or toxic transition metals.

Acknowledgements:

The authors thank M.-L. Doublet and C. Robert for DFT band gap calculations and D. Massiot, and F. Fayon for insightful discussions on NMR. The authors warmly acknowledge E. Suard and M. Avdeev for performing NPD diffraction experiments on the D2B beamline at ILL (Institute Laue-Langevin, Grenoble, France) and on the Echidna diffractometer, ANSTO (Australian Nuclear Science and Technology Organisation) respectively. A.M.A. thanks AICF of Skoltech for providing access to transmission electron microscopy equipment. J.-M.T. and B.L acknowledge funding from the European Research Council (ERC) (FP/2014)/ERC Grant-Project 670116-ARPEMA. This work used the 11-BM mail service of the Advanced Photon Source, a US Department of Energy (DOE) Office of Science User Facility operated for the DOE Office of Science by Argonne National Laboratory under contract no. DE-AC02-06CH11357. Financial support from the IR-RMN-THC Fr3050 CNRS for conducting the research is gratefully acknowledged.

(1) Delmas, C.; Fouassier, C.; Hagenmuller, P. Structural Classification and Properties of the Layered Oxides. *Phys. B+C* **1980**, *99* (1), 81–85. https://doi.org/https://doi.org/10.1016/0378-4363(80)90214-4.

(2) McCalla, E.; Abakumov, A. M.; Saubanère, M.; Foix, D.; Berg, E. J.; Rousse, G.; Doublet, M.-L.; Gonbeau, D.; Novák, P.; Van Tendeloo, G.; Dominko, R.; Tarascon, J.-M. Visualization of O-O Peroxo-like Dimers in High-Capacity Layered Oxides for Li-Ion Batteries. *Science (80-.).* **2015**, *350* (6267), 1516 LP – 1521. https://doi.org/10.1126/science.aac8260.

(3) Sathiya, M.; Abakumov, A. M.; Foix, D.; Rousse, G.; Ramesha, K.; Saubanère, M.; Doublet, M. L.; Vezin, H.; Laisa, C. P.; Prakash, A. S.; Gonbeau, D.; VanTendeloo, G.; Tarascon, J.-M. Origin of Voltage Decay in High-Capacity Layered Oxide Electrodes. *Nat. Mater.* **2015**, *14* (2), 230–238. https://doi.org/10.1038/nmat4137.

(4) Strobel, P.; Lambert-Andron, B. Crystallographic and Magnetic Structure of Li_2MnO_3. *J. Solid State Chem.* **1988**, *75* (1), 90–98. https://doi.org/https://doi.org/10.1016/0022-4596(88)90305-2.

(5) Mogare, K. M.; Friese, K.; Klein, W.; Jansen, M. Syntheses and Crystal Structures of Two Sodium Ruthenates: Na_2RuO_4 and Na_2RuO_3. *Zeitschrift für Anorg. und Allg. Chemie* **2004**, *630* (4), 547–552. https://doi.org/https://doi.org/10.1002/zaac.200400012.

(6) Bastow, T. J.; Hobday, M. E.; Smith, M. E.; Whitfield, H. J. Structural Characterisation of Na_2ZrO_3. *Solid State Nucl. Magn. Reson.* **1994**, *3* (2), 49–57. https://doi.org/https://doi.org/10.1016/0926-2040(94)90023-X.

(7) Ye, F.; Chi, S.; Cao, H.; Chakoumakos, B. C.; Fernandez-Baca, J. A.; Custelcean, R.; Qi, T. F.; Korneta, O. B.; Cao, G. Direct Evidence of a Zigzag Spin-Chain Structure in the Honeycomb Lattice: A Neutron and x-Ray Diffraction Investigation of Single-Crystal Na_2IrO_3. *Phys. Rev. B* **2012**, *85* (18), 180403.

(8) Perez, A. J.; Rousse, G.; Tarascon, J.-M. Structural Instability Driven by Li/Na Competition in $Na(Li_{1/3}Ir_{2/3})O_2$ Cathode Material for Li-Ion and Na-Ion Batteries. *Inorg. Chem.* **2019**, *58* (22), 15644–15651. https://doi.org/10.1021/acs.inorgchem.9b02722.

(9) Wang, Q.; Mariyappan, S.; Rousse, G.; Morozov, A. V; Porcheron, B.; Dedryvère, R.; Wu, J.; Yang, W.; Zhang, L.; Chakir, M.; Avdeev, M.; Deschamps, M.; Yu, Y.-S.; Cabana, J.; Doublet, M.-L.; Abakumov, A. M.; Tarascon, J.-M. Unlocking Anionic Redox Activity in O3-Type Sodium 3d Layered Oxides via Li Substitution. *Nat. Mater.* **2021**, *20* (3), 353–361. https://doi.org/10.1038/s41563-020-00870-8.

(10) Colombet, P.; Danot, M.; Jumas, J.-C.; Philippot, E. Sur Les Systèmes TiS_2 - A_2S (A= Na et K). *Comptes rendus Hebd. des séances l'Académie des Sci. Série C, Sci. Chim.* **1978**, *287*, 411.

(11) Mark, W.; Lindqvist, O.; Jumas, J.-C.; Philippot, E. The OD Structure of Na_2SnS_3. Determination and Refinement of an MDO Structure. *Acta Crystallogr. Sect. B* **1974**, *30* (11), 2620–2628.

(12) Pelé, V. Nouveaux Matériaux d'électrodes Pour Microbatteries Au Sodium, Université de Bordeaux, 2016.

(13) Nasu, A.; Otoyama, M.; Sakuda, A.; Hayashi, A.; Tatsumisago, M. Amorphous Na_2TiS_3 as an Active Material for All-Solid-State Sodium Batteries. *Chem. Lett.* **2019**, *48* (3), 288–290. https://doi.org/10.1246/cl.180895.

(14) Nasu, A.; Otoyama, M.; Sakuda, A.; Hayashi, A.; Tatsumisago, M. Mechanochemical Synthesis of Cubic Rocksalt Na_2TiS_3 as Novel Active Materials for All-Solid-State Sodium Secondary Batteries. *J. Ceram. Soc. Japan* **2019**, *127* (8), 514–517. https://doi.org/10.2109/jcersj2.19086.

(15) Flamary-Mespoulie, F.; Boulineau, A.; Martinez, H.; Suchomel, M. R.; Delmas, C.; Pecquenard, B.; Le Cras, F. Lithium-Rich Layered Titanium Sulfides: Cobalt- and Nickel-Free High Capacity Cathode Materials for Lithium-Ion Batteries. *Energy Storage Mater.* **2020**, *26*, 213–222. https://doi.org/https://doi.org/10.1016/j.ensm.2019.12.033.

(16) Furuseth, S.; Brattås, L.; Kjekshus, A.; Andresen, A. F.; Fischer, P. On the Crystal Structures of TiS_3, ZrS_3, $ZrSe_3$, $ZrTe_3$, HfS_3, and $HfSe_3$. *Acta Chem. Scand* 623–631.

(17) Gorochov, O.; Katty, A.; Le Nagard, N.; Levy-Clement, C.; Schleich, D. M. Photoelectrochemical Study of TiS_3 in Aqueous Solution. *Mater. Res. Bull.* **1983**, *18* (1), 111–118. https://doi.org/https://doi.org/10.1016/0025-5408(83)90178-2.

(18) Buerger, M. J. Interatomic Distances in Marcasite and Notes on the Bonding in Crystals of Löllingite, Arsenopyrite, and Marcasite Types. *Zeitschrift für Krist. - Cryst. Mater. 97* (1), 504–513. https://doi.org/https://doi.org/10.1524/zkri.1937.97.1.504.

(19) Folmer, J. C. W.; Jellinek, F.; Calis, G. H. M. The Electronic Structure of Pyrites, Particularly CuS_2 and $Fe_{1-x}Cu_xSe_2$: An XPS and Mössbauer Study. *J. Solid State Chem.* **1988**, *72* (1), 137–144. https://doi.org/https://doi.org/10.1016/0022-4596(88)90017-5.

(20) Li, B.; Jiang, N.; Huang, W.; Yan, H.; Zuo, Y.; Xia, D. Thermodynamic Activation of Charge Transfer in Anionic Redox Process for Li-Ion Batteries. *Adv. Funct. Mater.* **2018**, *28* (4), 1704864. https://doi.org/https://doi.org/10.1002/adfm.201704864.

(21) Saha, S.; Assat, G.; Sougrati, M. T.; Foix, D.; Li, H.; Vergnet, J.; Turi, S.; Ha, Y.; Yang, W.; Cabana, J.; Rousse, G.; Abakumov, A. M.; Tarascon, J.-M. Exploring the Bottlenecks of Anionic Redox in Li-Rich Layered Sulfides. *Nat. Energy* **2019**, *4* (11), 977–987. https://doi.org/10.1038/s41560-019-0493-0.

(22) Sakuda, A.; Takeuchi, T.; Okamura, K.; Kobayashi, H.; Sakaebe, H.; Tatsumi, K.; Ogumi, Z. Rock-Salt-Type Lithium Metal Sulphides as Novel Positive-Electrode Materials. *Sci. Rep.* **2014**, *4* (1), 4883. https://doi.org/10.1038/srep04883.

(23) Leube, B. T.; Robert, C.; Foix, D.; Porcheron, B.; Dedryvère, R.; Rousse, G.; Salager, E.; Cabelguen, P.-E.; Abakumov, A. M.; Vezin, H.; Doublet, M.-L.; Tarascon, J.-M. Activation of Anionic Redox in d^0 Transition Metal Chalcogenides by Anion Doping. *Nat. Commun.* **2021**, *12* (1), 5485. https://doi.org/10.1038/s41467-021-25760-8.

(24) Leube, B. T.; Suard, E. Structure Solution of Novel Na-Ti-S Phase. Institut Laue-Langevin (ILL). **2021**. https://doi.org/10.5291/ILL-DATA.EASY-873.

(25) Lissner, F.; Schleid, T. Na_2ZrS_3: Ein Ternäres Sulfid Des Zirconiums Mit Aufgefüllter $AlCl_3$-Struktur. *Zeitschrift für Anorg. und Allg. Chemie* **1999**, *625* (2), 195–196. https://doi.org/https://doi.org/10.1002/(SICI)1521-3749(199902)625:2<195::AID-ZAAC195>3.0.CO;2-V.

(26) Harringer, N. A.; Kolb, A.; Klepp, K. O. Na_2ZrSe_3, Ein Neues Chalcogenometallat(IV) Mit Schichtstruktur/Na_2ZrSe_3, a New Chalcogenometallate(IV) with a Layered Structure. *Zeitschrift für Naturforsch. B* **2001**, *56* (12), 1322–1324. https://doi.org/doi:10.1515/znb-2001-1212.

(27) Liu, J.; Yin, L.; Wu, L.; Bai, J.; Bak, S.-M.; Yu, X.; Zhu, Y.; Yang, X.-Q.; Khalifah, P. G. Quantification of Honeycomb Number-Type Stacking Faults: Application to $Na_3Ni_2BiO_6$ Cathodes for Na-Ion Batteries. *Inorg. Chem.* **2016**, *55* (17), 8478–8492. https://doi.org/10.1021/acs.inorgchem.6b01078.

(28) Saha, S. Exploration of Ionic Conductors and Li-Rich Sulfides for All-Solid-State Batteries, 2020.

(29) Martinolich, A. J.; Zak, J. J.; Agyeman-Budu, D. N.; Kim, S. S.; Bashian, N. H.; Irshad, A.; Narayan, S. R.; Melot, B. C.; Nelson Weker, J.; See, K. A. Controlling Covalency and Anion Redox Potentials through Anion Substitution in Li-Rich Chalcogenides. *Chem. Mater.* **2021**, *33* (1), 378–391. https://doi.org/10.1021/acs.chemmater.0c04164.

(30) Chianelli, R. R.; Dines, M. B. Reaction of Butyllithium with Transition Metal Trichalcogenides. *Inorg. Chem.* **1975**, *14* (10), 2417–2421. https://doi.org/10.1021/ic50152a023.

(31) Ōnuki, Y.; Inada, R.; Tanuma, S.; Yamanaka, S.; Kamimura, H. Electrochemical Characteristics of Transition-Metal Trichalcogenides in the Secondary Lithium Battery. *Solid State Ionics* **1983**, *11* (3), 195–201. https://doi.org/https://doi.org/10.1016/0167-2738(83)90024-3.

(32) Holleck, G. L.; Driscoll, J. R. Transition Metal Sulfides as Cathodes for Secondary Lithium Batteries—II. Titanium Sulfides. *Electrochim. Acta* **1977**, *22* (6), 647–655. https://doi.org/https://doi.org/10.1016/0013-4686(77)85134-7.

(33) Murphy, D. W.; Trumbore, F. A. The Chemistry of TiS_3 and $NbSe_3$ Cathodes. *J. Electrochem. Soc.* **1976**, *123* (7), 960–964. https://doi.org/10.1149/1.2133012.

(34) Murphy, D. W.; Trumbore, F. A. Metal Chalcogenides as Reversible Electrodes in Nonaqueous Lithium Batteries. *J. Cryst. Growth* **1977**, *39* (1), 185–199. https://doi.org/https://doi.org/10.1016/0022-0248(77)90165-8.

(35) Huang, F. Q.; Yao, J.; Liu, Z.; Yang, J.; Ibers, J. A. Synthesis, Structure, and Ionic Conductivity of $Na_5Li_3Ti_2S_8$. *J. Solid State Chem.* **2008**, *181* (4), 837–841. https://doi.org/https://doi.org/10.1016/j.jssc.2008.01.023.

(36) House, R. A.; Maitra, U.; Pérez-Osorio, M. A.; Lozano, J. G.; Jin, L.; Somerville, J. W.; Duda, L. C.; Nag, A.; Walters, A.; Zhou, K.-J.; Roberts, M. R.; Bruce, P. G. Superstructure Control of First-Cycle Voltage Hysteresis in Oxygen-Redox Cathodes. *Nature* **2020**, *577* (7791), 502–508. https://doi.org/10.1038/s41586-019-1854-3.

(37) Dorrian, J. F.; Newnham, R. E. Refinement of the Structure of Li_2TiO_3. *Mater. Res. Bull.* **1969**, *4* (3), 179–183. https://doi.org/https://doi.org/10.1016/0025-5408(69)90054-3.

(38) Meng, F.; Liu, Y.; Xue, T.; Su, Q.; Wang, W.; Qi, T. Structures, Formation Mechanisms, and Ion-Exchange Properties of α-, β-, and γ-Na_2TiO_3. *RSC Adv.* **2016**, *6* (113), 112625–112633. https://doi.org/10.1039/C6RA16984H.

The layered sodium titanium trichalcogenide Na_2TiCh_3 framework (*Ch*= S, Se): A rich crystal and electrochemical chemistry.

Bernhard T. Leube[1,2], Elodie Salager[2,3], Erwan Chesneau[2,3], Gwenaëlle Rousse[1,2,4], Hervé Vezin[5], Artem M. Abakumov[6] and Jean-Marie Tarascon[1,2]

[1] Collège de France, Chaire de Chimie du Solide et de l'Energie, UMR 8260, 11 Place Marcelin Berthelot, 75231 CEDEX 05 Paris, France
[2] Réseau sur le Stockage Electrochimique de l'Energie (RS2E), FR CNRS 3459, 33 Rue Saint Leu, 80039 Amiens, France
[3]CNRS, CEMHTI, UPR3079, Université d'Orléans, 1D avenue de la recherche scientifique, Orléans, France
[4]Sorbonne Université, 4 Place Jussieu, F-75005 Paris, France
[5]Université Lille Nord de France, CNRS UMR8516, LASIRE, Villeneuve d'Ascq, France
[6]Center for Energy Science and Technology, Skolkovo Institute of Science and Technology, Nobel str. 3, 121205 Moscow, Russia

Synthesis.

General procedure. Due to the water/air sensitivity of sulfides, all sample manipulations were executed in glove boxes. The commercially available reagents TiS_2 (Sigma-Aldrich, 99.9%) and Na_2S (Sigma-Aldrich) were used as received from the vendors. All other reagents (Li_2S, Na_2Se, $TiSe_2$, ZrS_2 and $ZrSe_2$) were synthesized in-house as described in the following section. The title compounds $Na_{2-x}Li_xTiS_3$ (*x*= 0, 0.5, 1.0, 1.5) and Na_2TMCh_3 (*TM*= Ti, Zr; *Ch*= S, Se) were prepared by hand-grinding the reagents in appropriate stoichiometric ratios, consecutive sealing in evacuated quartz tubes under vacuum ($p < 10^{-4}$ mbar) as powder and high-temperature calcination. The appropriate heating temperature *T* and time *t* were investigated for each targeted composition, giving the following optimized parameters (*n. b.* the minimal time *t* necessary for full completion of the reaction was not subject of the optimization):

	Temperature *T*/ K	Time *t*/ h
Na_2TiS_3	773	48
$Na_{1.5}[Li_{0.5}Ti]S_3$	773	36
Na_2TiSe_3	673	36
Na_2ZrS_3	973	72
Na_2ZrSe_3	773	72

Li_2S. Lithium sulfide was synthesized by heating lithium carbonate (Li_2CO_3, Sigma-Aldrich, > 99%) under a stream of argon/CS_2 (Sigma-Aldrich) vapor at 923 K for 5 h.

Na_2Se. Sodium selenide was synthesized by mechanically mixing Na metal and Se powder using a Fritsch pulverisette 7 planetary ball mill (typically 3g, 10 10-mm ZrO_2 balls in a 80 mL ZrO_2 jar, 10 h, 500 rpm).

$TiSe_2$. Titanium selenide was synthesized by heating titanium (Ti, Sigma-Aldrich, 99. 98%) and selenium powder (Se, Alfa Aesar, 99.999%) in an evacuated quartz tube at 673 K for 12 h.

$ZrCh_2$ (*Ch*= S, Se). Zirconium chalcogenides were synthesized by heating zirconium wire (Zr, Alfa Aesar, 99.2%) with sulphur (S, Sigma-Aldrich, 99.98%) or selenium powder at 1273 K for 12 h applying a very low heating rate of 0.5 K/min.

Chemical desodiation of Na_2TiS_3. Na_2TiS_3 (100 mg, 0.526 mmol) and iodine (I_2, 133.6 mg, 0.626 mmol, 1.2 eq) were dispersed in 10 mL Acetonitrile and stirred at ambient temperature for 20 h. The reaction product Na_xTiS_3 was separated by centrifugation, washed with Acetonitrile (3x 10 mL) and finally dried under vacuum.

$Na_{1.5}[Li_{0.5}Ti]O_3$. Li_2CO_3 (276.1 mg, 3.74 mmol, Sigma, > 99%), Na_2CO_3 (1188.0 mg, 11.2 mmol, Alfa Aesar, 99%) and TiO_2 (Anatase, 1193.6 mg, 14.95 mmol, Alfa Aesar, nanopowder, > 99.7%) were thoroughly hand ground in a pestle and mortar and calcined in an alumina crucible at 923 K for 12 h.

Characterization.

X-ray powder diffraction. High resolution synchrotron X-ray diffraction (SXRD) patterns were recorded at the Cristal beamline of the Soleil synchrotron (λ= 0.58185 Å) or at the 11-BM of the Advanced Photon Source (APS), Argonne National Laboratory (λ= 0.457889 Å). The samples were sealed in quartz capillaries (r_{cap}= 0.3 mm) and measured in transmission mode. For in house powder X-ray diffraction (PXRD) experiments samples were enclosed in an airtight electrochemical cell with a Be window. The data was collected in reflection mode in Bragg-Brentano geometry using a Bruker D8 Advance diffractometer equipped with a Cu-K_α source (λ_1= 1.54056 Å, λ_2= 1.54439 Å) and a LynxEye detector. Analysis and refinements of the as collected diffraction patterns were carried out using the FullProf program suite.

Neutron powder diffraction. A constant wavelength neutron powder diffraction (NPD) pattern of approximately 1.7 g pristine Na_2TiS_3 was recorded on the D2B diffractometer, Institut Laue-Langevin, while 2 g of pristine $Na_{1.5}[Li_{0.5}Ti]S_3$ was measured on the Echidna diffractometer, ANSTO (Australian Nuclear Science and Technology Organisation).

Electrochemical characterization. To prepare the cathode active material $Na_{2-x}Li_xTmCh_3$ (*Tm*= Ti, Zr; *Ch*= S, Se) was thoroughly mixed and ground with 15 wt% conductive carbon (Csp). Typical Swagelok-type cells with loadings of 5-10 mg of the cathode material, Whatman GF/D borosilicate glass fiber membranes as the separator, electrolyte (250-500 µL) and a metallic anode were assembled in an Ar-filled glovebox. For cycling against Li, Li ribbon was used as the anode in combination with LP30 as the electrolyte (1 M $LiPF_6$ in dimethylcarbonate/ethylenecarbonate (1:1)). In the case of cycling against Na, metallic Na was used as the anode with 1 M $NaPF_6$ in propylenecarbonate as the electrolyte. The cells were allowed to rest for 30 min and were then galvanostatically cycled at *C/*10 rate, corresponding to the removal of 1 Li per formula unit in 10h. For *ex-situ* experiments the cathode materials were recovered after cycling, washed with dimethylcarbonate (DMC, Sigma-Aldrich, >99%) and dried under vacuum. Galvanostatic intermittent titration technique (GITT) experiments were run on the second electrochemical cycle of the respective material with galvanostatic pulses at rates of *C/10* for 1.5 h followed by a 4 h open circuit step.

EPR. Room temperature and 110K X-Band EPR measurement were performed with a Bruker ELEXSYS E500. The spectra were recorded with 5mW microwave power and 2 G for amplitude modulation.

TEM. TEM samples were prepared by dispersing the powder in DMC (dimethyl carbonate) in an agate mortar and depositing drops of this suspension onto a carbon film supported by a copper grid. The samples were transferred from the Ar-filled glove box to the microscope column using a Gatan vacuum transfer holder completely excluding contact with air. Electron diffraction (ED) patterns, high-angle annular dark-field scanning transmission electron microscopy (HAADF-STEM) images and scanning transmission electron microscopy (STEM-EDX) compositional maps were acquired on a probe aberration-corrected Titan Themis Z electron microscope operated at 200 kV and equipped with a Super-X system for energy-dispersive X-ray (EDX) analysis.

NMR. ^{23}Na NMR experiments for the Na_2TiS_3 pristine, charged and discharged (against Li^+/Li) samples were conducted using a Bruker Avance III with a magnetic field of 4.7 T to increase the quadrupolar effect on the spectrum and better separate the sites. The spectra display signals with quadrupolar lineshapes that constrain the fits better. The NMR spectra were recorded using a Bruker 1.3 mm double resonance HX Bruker MAS probe spinning the rotors at the magic angle at a rate of 62.5 kHz. RF nutation was strongly influenced by the quadrupolar interaction; a strong and short pulse was used for quantitativity (π/18 at 50 W). The repetition time was adapted to be longer than 5 times the

longitudinal relaxation time and the number of co-added transients was 348, 8192 and 4096, for respectively. For $Na_{1.5}Li_{0.5}TiS_3$ 2240 transients were coadded. (Figure 8a,b,e).

The quantification of the ^{23}Na NMR for the $Na_{1.5}Li_{0.5}TiS_3$ series (pristine, charged and discharged) was conducted on a Bruker Avance III with a magnetic field of 17.6 T, using a Bruker 1.3 mm double resonance HX MAS probe. The rotor for the charged sample could not be spun faster than 60 kHz hence all samples were measured at that spinning rate. Pi/18 pulses were used at 30 W (87 kHz on the liquid reference) and the repetition time was adjusted to ensure quantitativity. 128 or 384 transients were coadded. The spectra were referenced to a 1 $mol \cdot L^{-1}$ aqueous NaCl solution at 0 ppm (Figure 8f).

The ^{7}Li NMR spectra of all samples (Figure 8g,h) were recorded in the high-field spectrometers, using the same Bruker 1.3 mm HX probe, with a single pulse at 30 W (102 kHz on the liquid reference no quadrupolar effect detected). The spectra were processed with an exponential apodization (line broadening of 5 Hz) and referenced to a 1 $mol \cdot L^{-1}$ aqueous LiCl solution at 0 ppm.

A home-made MATLAB script (MathWorks) was used to open the data and integrate the ^{23}Na and ^{7}Li NMR spectra. The central transition and the n=0 band of the satellite transitions were integrated together, as the broader lines prevent spectral selection. Tests on the pristine materials indicate that it creates an error of ~2% on the measurements.

We considered that the pristine contained 2 Na and 1.5Na0.5Li per unit formula to calibrate the pristine samples, the other samples were calibrated related to the pristine samples. The areas were corrected for the mass of the sample contained in the rotors.

Figures

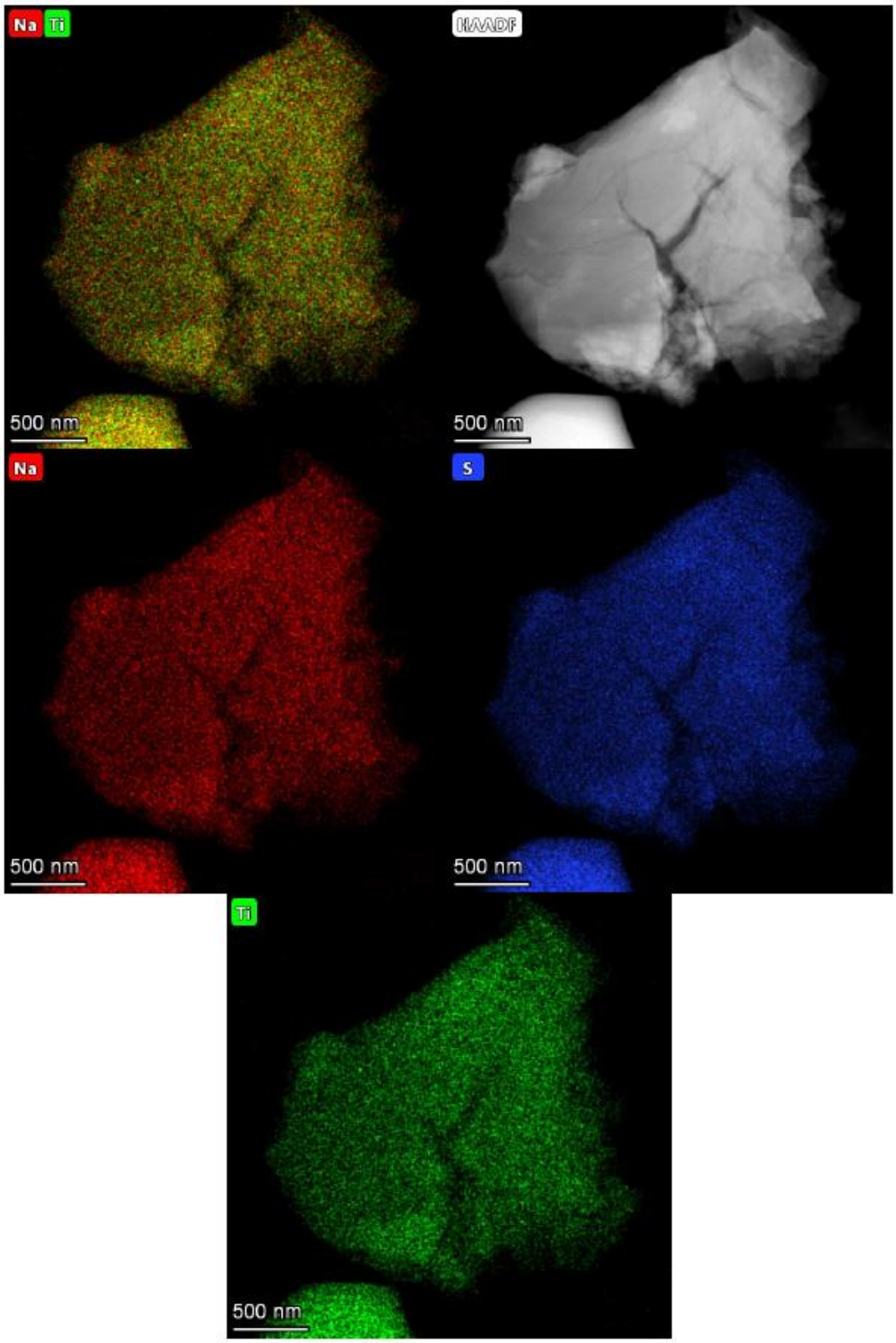


Figure S1: HAADF-STEM image of Na_2TiS_3, the corresponding EDX elemental maps for Na, Ti and S, and the mixed color-coded compositional map.

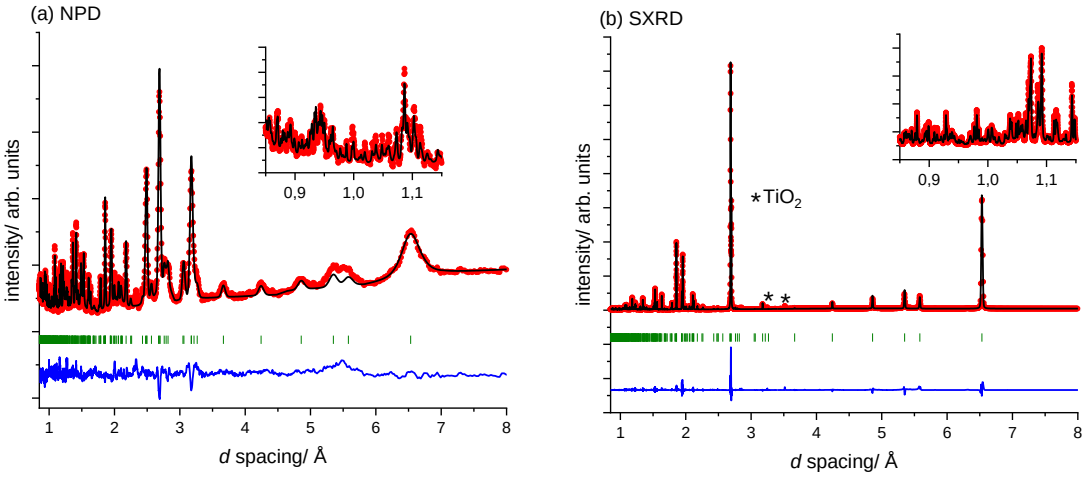
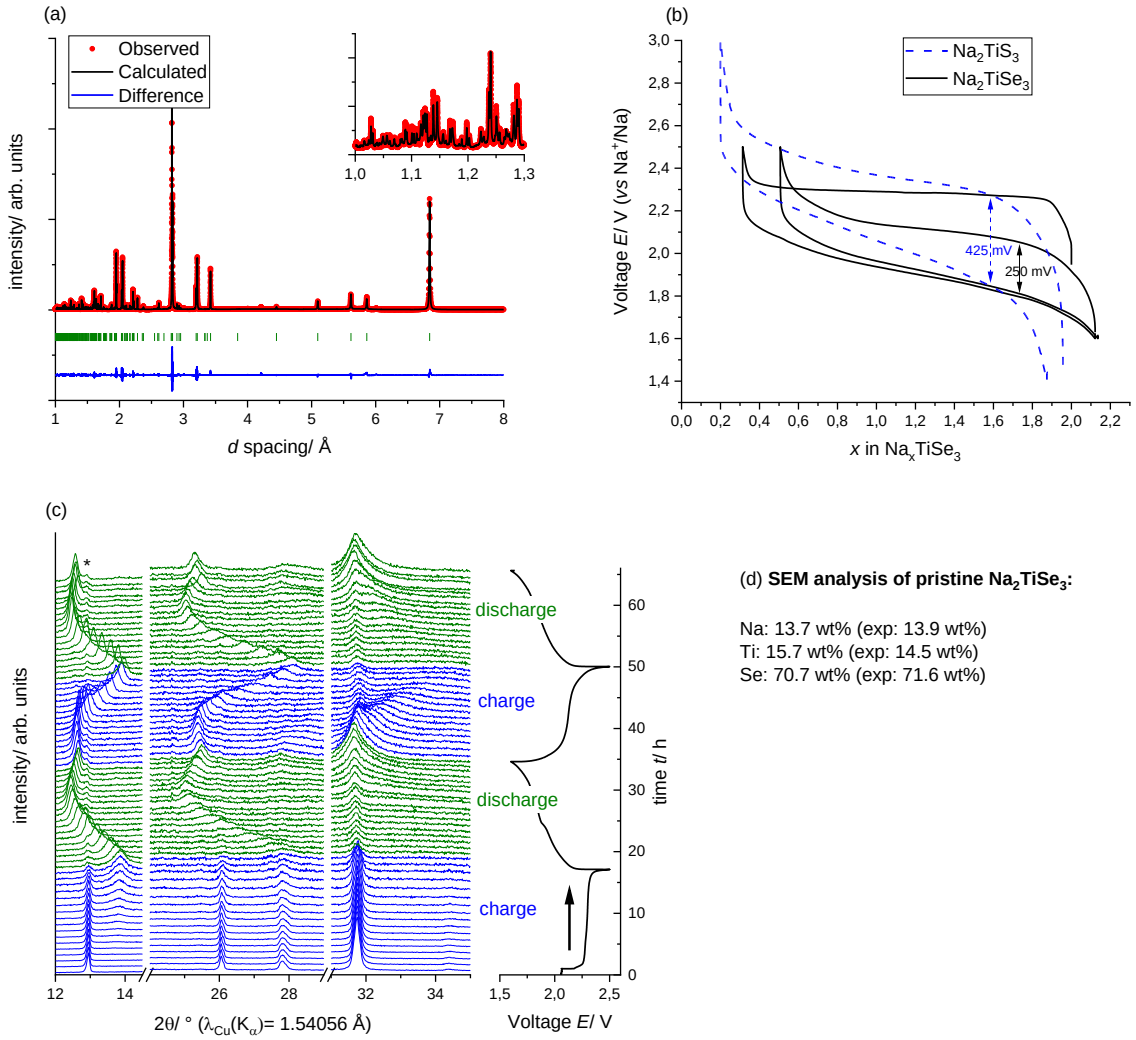


*Figure S2: Combined Rietveld refinement of pristine Na_2TiS_3 using (a) NPD and (b) SXRD data at RT. TiO_2 impurities are marked by asterisks *.*



(d) **SEM analysis of pristine Na_2TiSe_3:**

Na: 13.7 wt% (exp: 13.9 wt%)
Ti: 15.7 wt% (exp: 14.5 wt%)
Se: 70.7 wt% (exp: 71.6 wt%)

*Figure S3: Structural characterization of Na_2TiSe_3: (a) Rietveld refinement based on SXRD data (b) cycled against Na^+/Na (c) operando PXRD experiment vs Na^+/Na, a small amount pristine Na_2TiSe_3 was not in electrical contact with the cell and persists throughout the patterns (marked by an asterisk *). (d) result of a SEM analysis.*

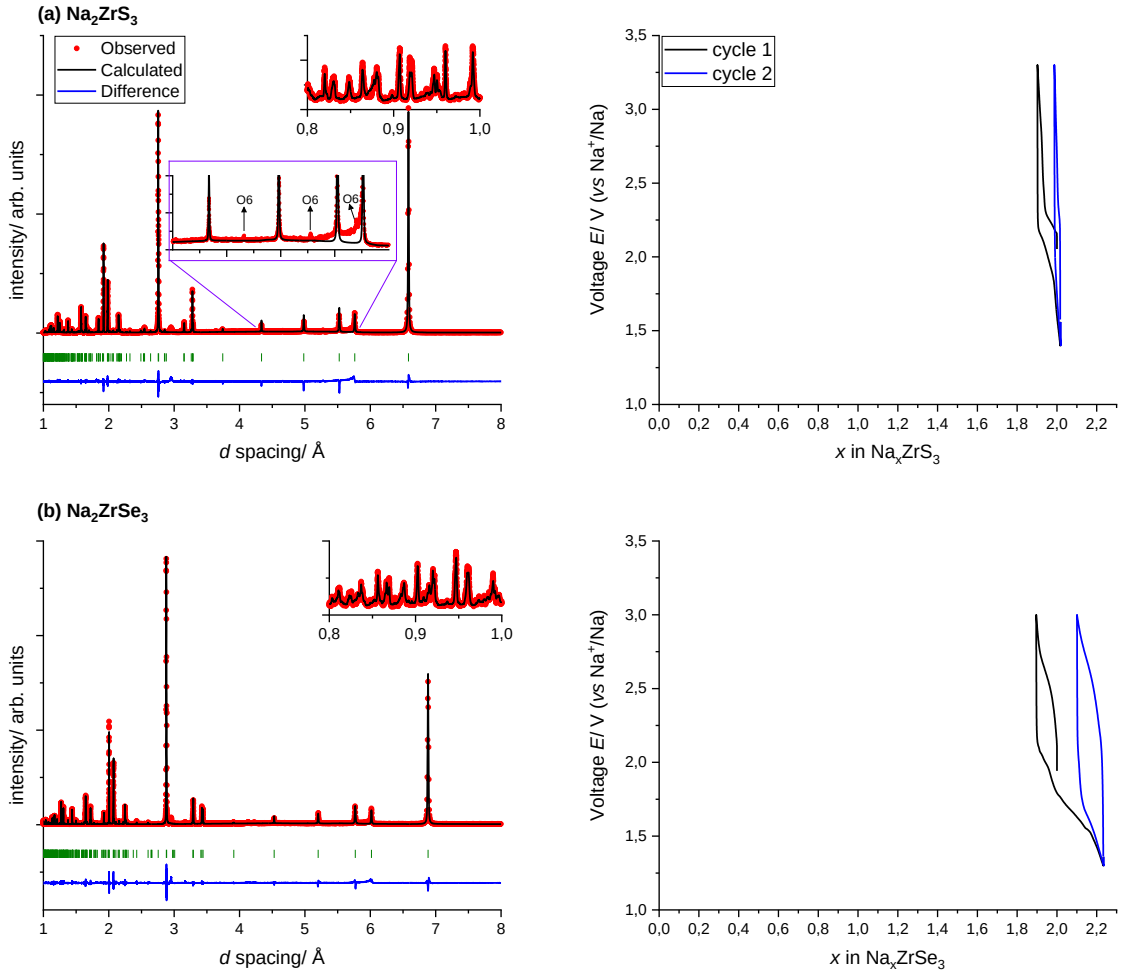


Figure S4: Structure and electrochemistry of (a) Na_2ZrS_3 and (b) Na_2ZrSe_3. The structural model of each phase was refined by the Rietveld method using SXRD data.

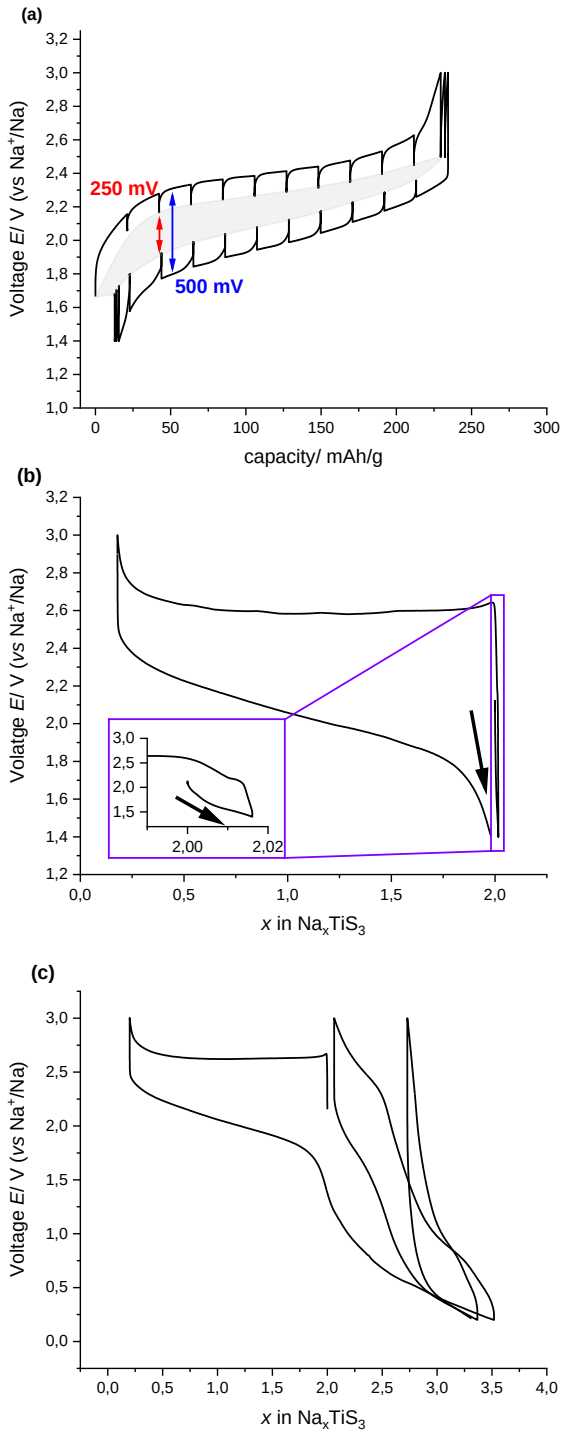


Figure S5: Electrochemistry of Na_2TiS_3 vs Na^+/Na. (a) 2nd cycle of a GITT experiment (b) cell started on discharge (c) galvanostatic cycling with an increased potential window from 3.0 V- 0.2 V.

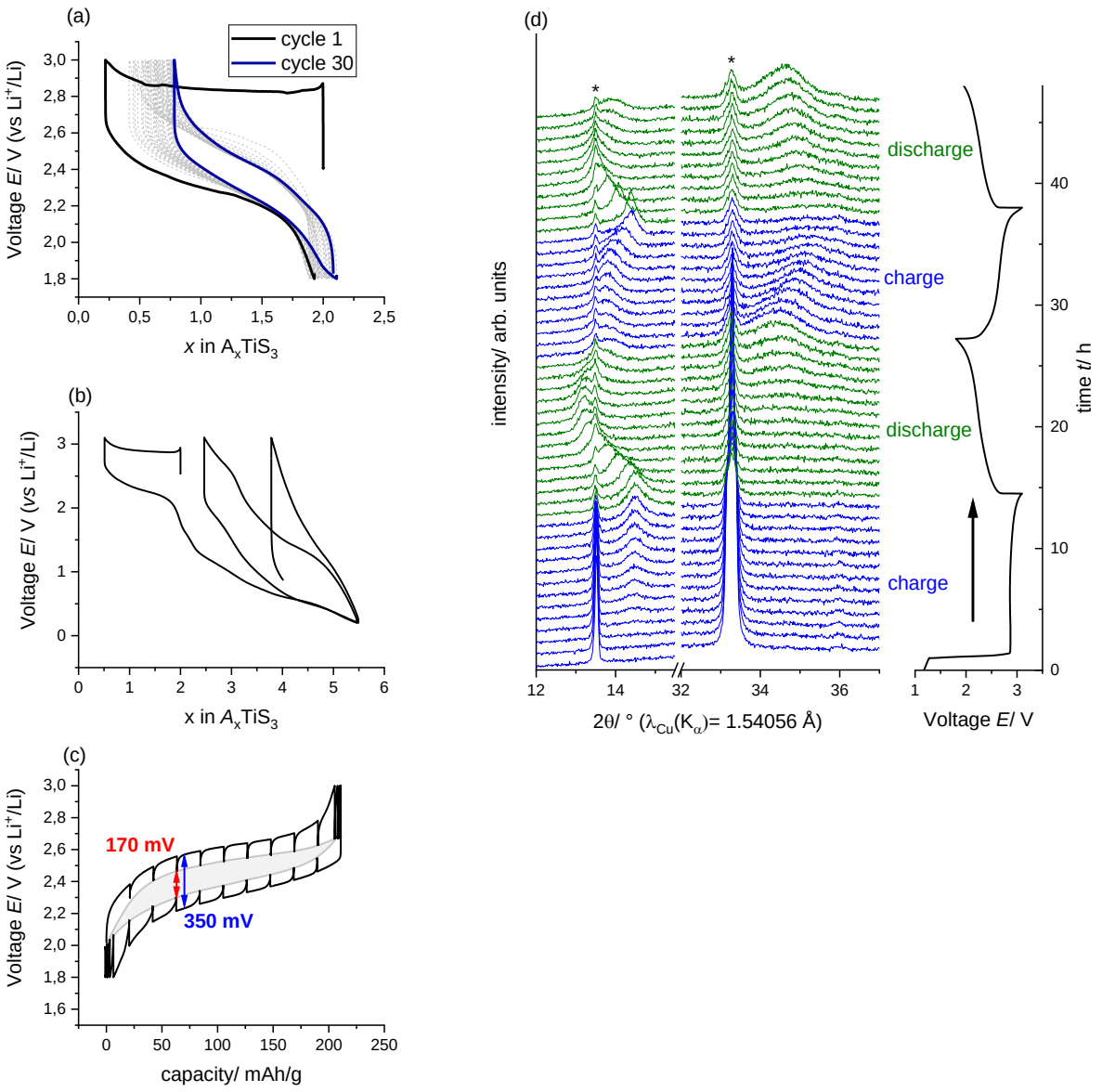


*Figure S6: Electrochemical experiments of Na_2TiS_3 cycled against **Li^+/Li** (a) 30 galvanostatic cycles (b) Na_2TiS_3|Li cell cycled from 3.1 V- 0.2 V (c) 2nd cycle of a GITT experiment (d) PXRD operando experiment of a Na_2TiS_3|Li cell, a small amount pristine Na_2TiS_3 was not in electrical contact with the cell and persists throughout the patterns (marked by an asterisk *).*

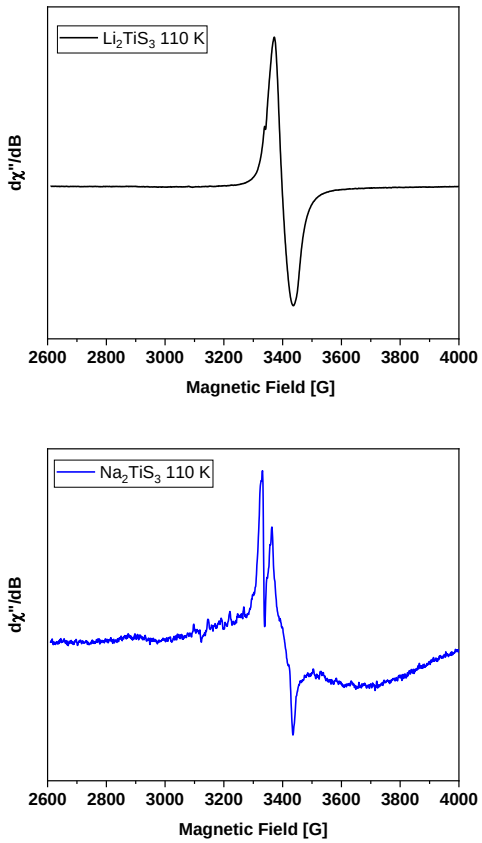


Figure S7: EPR measurement of Li_2TiS_3 (black) and Na_2TiS_3 (blue) at 110 K.

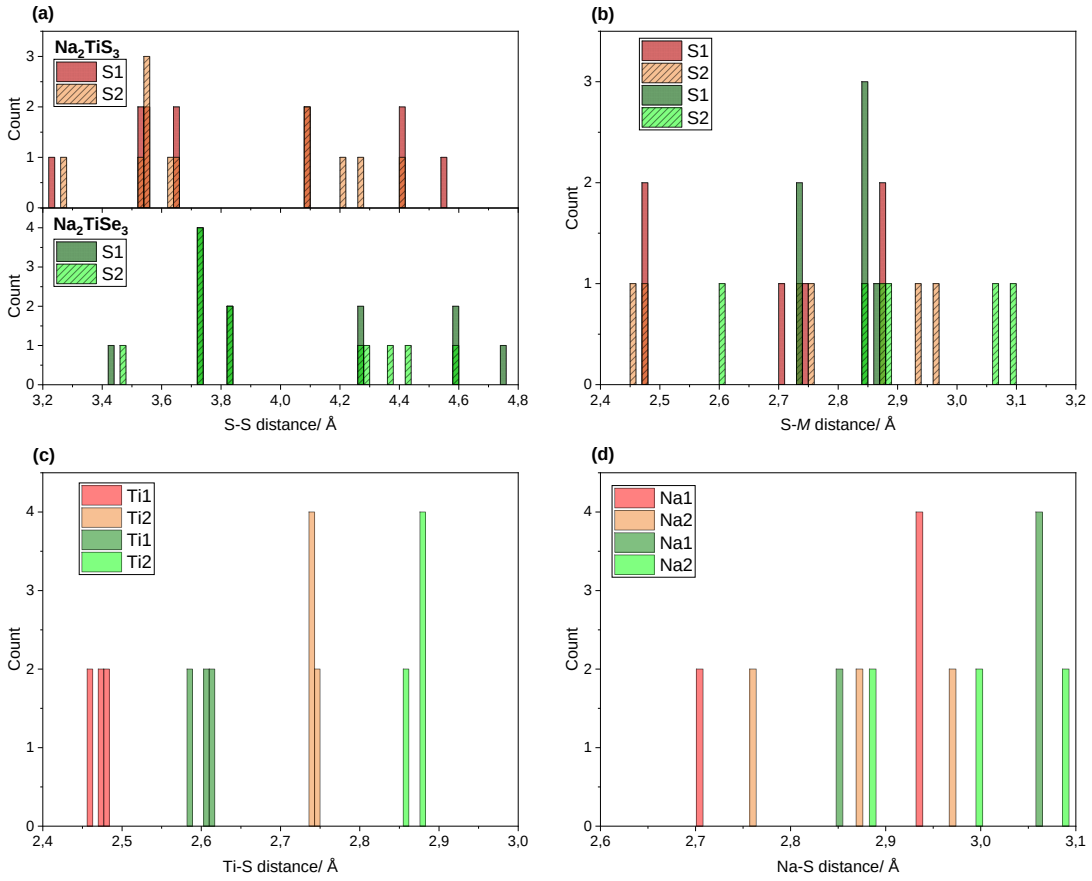


Figure S8 : Analysis of interatomic distances in Na_2TiS_3 compared to Na_2TiSe_3 based on the Rietveld-refined structures. (a) distance between a given chalcogenide atom in the "cubic" close-packed anion sublattice and its 12 nearest neighbors. (b) bond lengths in a given ChM_6 octahedron. (c) bond lengths in a given MCh_6 octahedron. (d) bond lengths in a given $NaCh_6$ octahedron. Color code: red: Na_2TiS_3, green: Na_2TiSe_3.

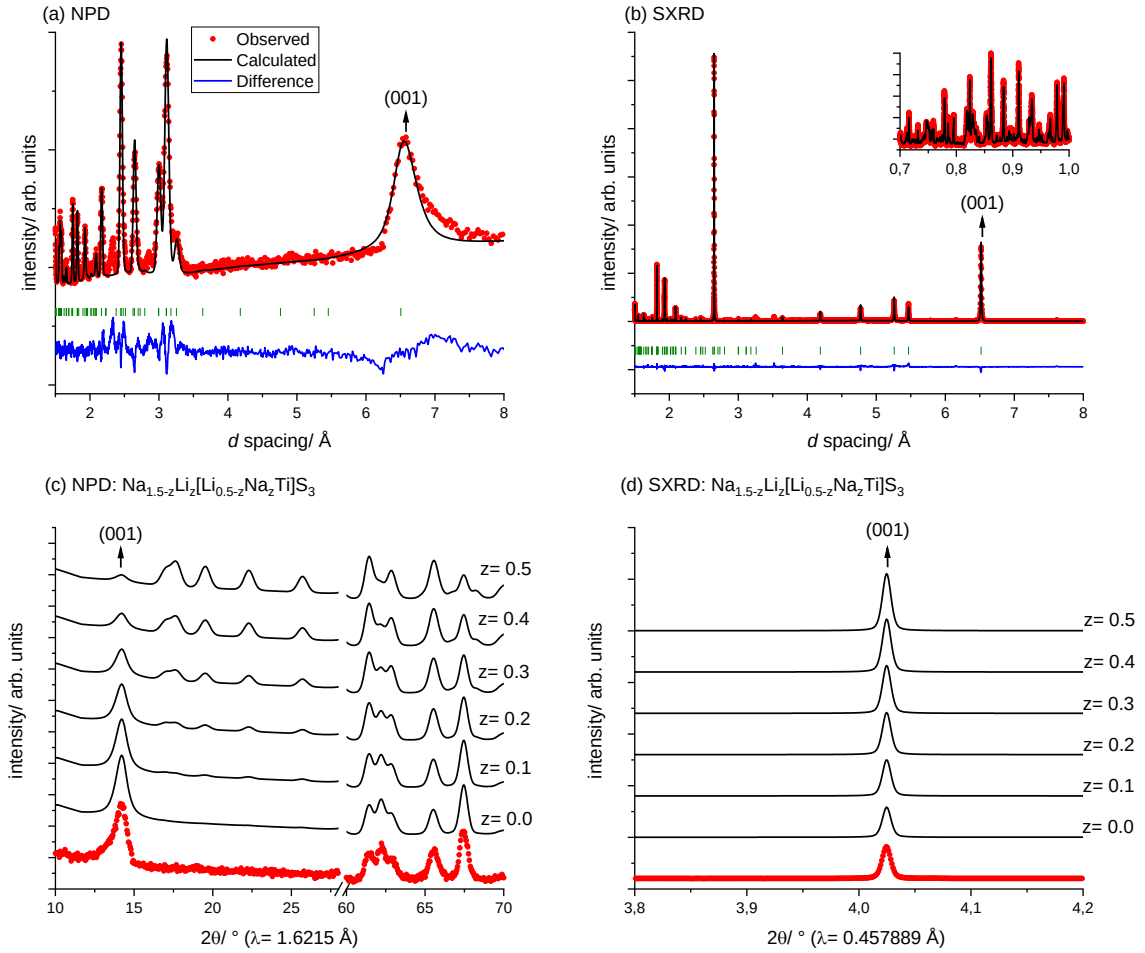


Figure S9: Diffraction experiments on $Na_{1.5}[Li_{0.5}Ti]S_3$. Combined Rietveld refinement of (a) NPD and (b) SXRD data. (space group $R\bar{3}m$, composition fixed to the nominal stoichiometry). Panels (c) and (d) show simulated NPD and SXRD patterns, respectively, for the $Na_{1.5-z}Li_z[Li_{0.5-z}Na_zTi]S_3$ series to compare the degree of Li vs Na mixing. The best agreement is observed when Li and Na do not mix at all (z= 0.0).

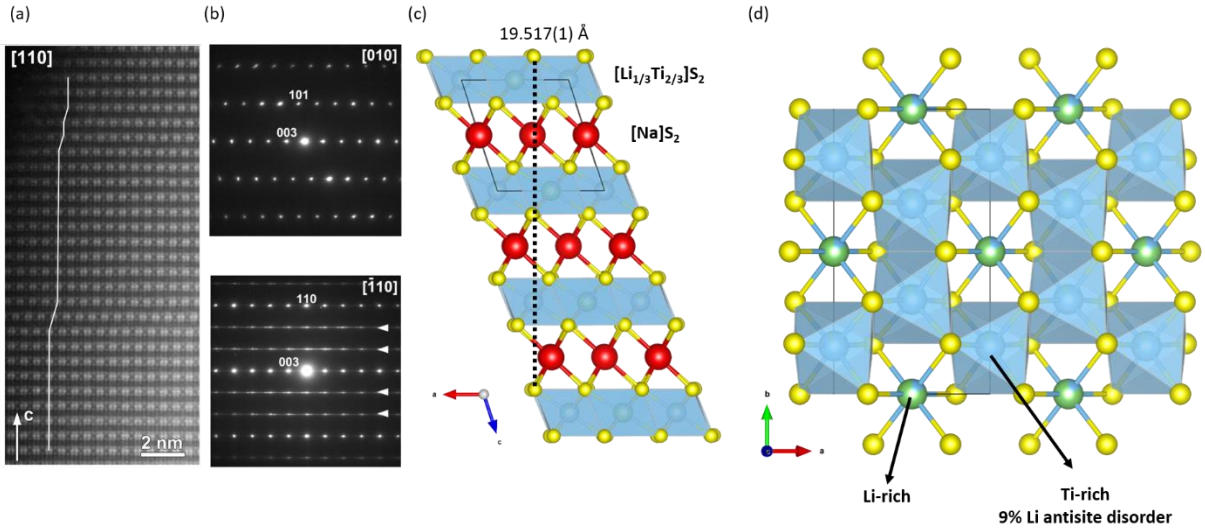


Figure S10: Structural characterization of $Na_{1.5}[Li_{0.5}Ti]S_3$.(a) [110] HAADF-STEM image, stacking faults along c are visible by random lateral displacements of the $[Li_{1/3}Ti_{2/3}]S_2$ blocks traced with zig-zag lines. (b) ED patterns indexed with the $R\bar{3}m$ space group, extra reflections and diffuse intensity due to the Li-Ti "honeycomb" ordering are marked with arrowheads. (c) structure as obtained from a combined SXRD-NPD Rietveld refinement viewed along the b axis, forming an O3 type structure. (d) Li-Ti "honeycomb" ordering in the mixed $[Li_{1/3}Ti_{2/3}]S_2$ slabs.

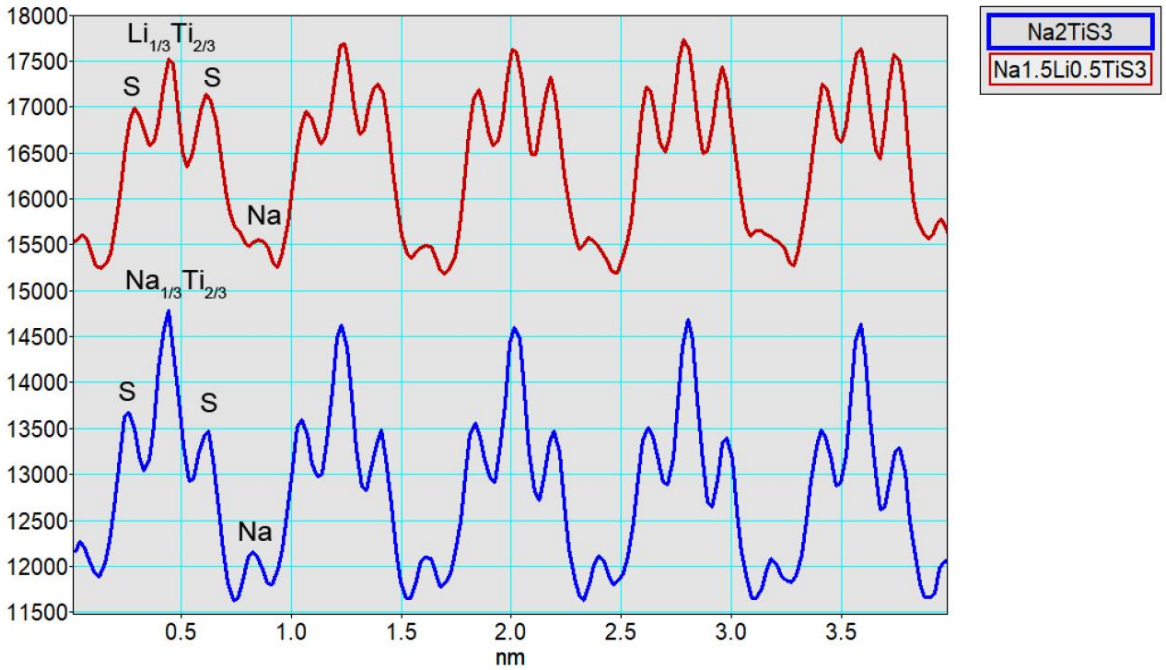


Figure S11: HAADF intensity profiles measured in the [010] HAADD-STEM image along the S-$A_{1/3}Ti_{2/3}$-S columns in the $Na_{1.5}Li_{0.5}TiS_3$ (red) and Na_2TiS_3 (blue) structures. Note the lower HAADF intensity at the $Li_{1/3}Ti_{2/3}$ sites compared to that at the $Na_{1/3}Ti_{2/3}$ ones.

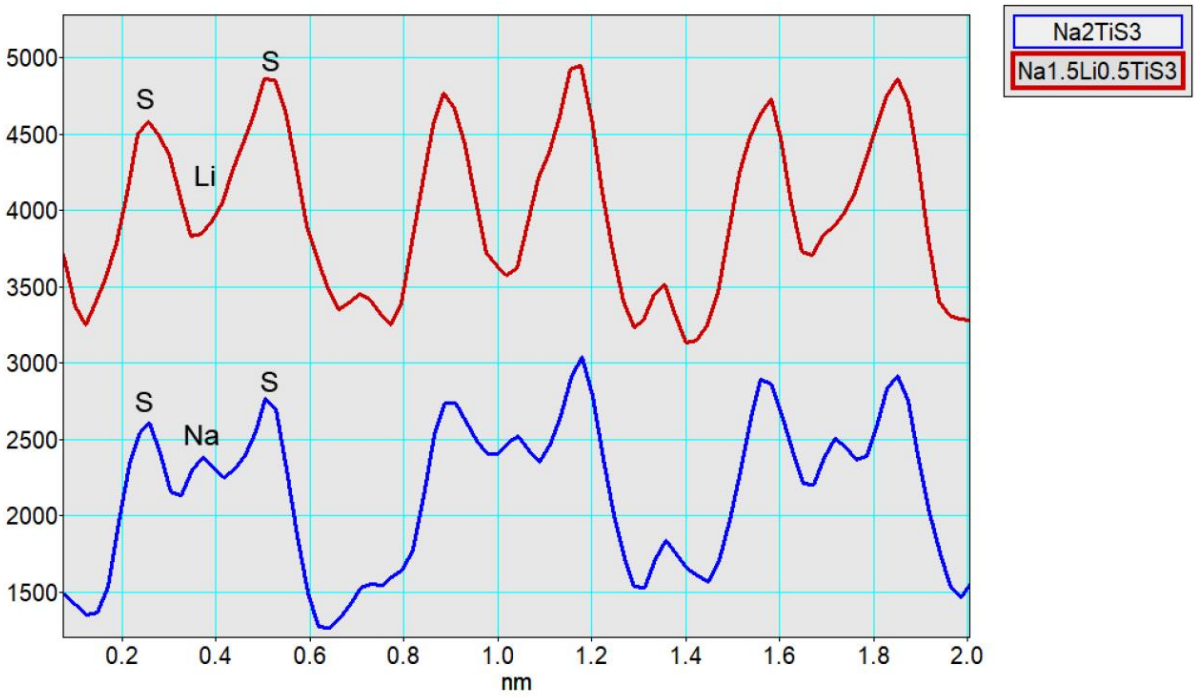


Figure S12: HAADF intensity profiles measured in the [110] HAADF-STEM image along the S-A-S columns in the $(A_{1/3}Ti_{2/3})S_2$ blocks of the $Na_{1.5}Li_{0.5}TiS_3$ (red) and Na_2TiS_3 (blue) structures. Note the lower HAADF intensity of the A sites occupied by Li compared to those occupied by Na.

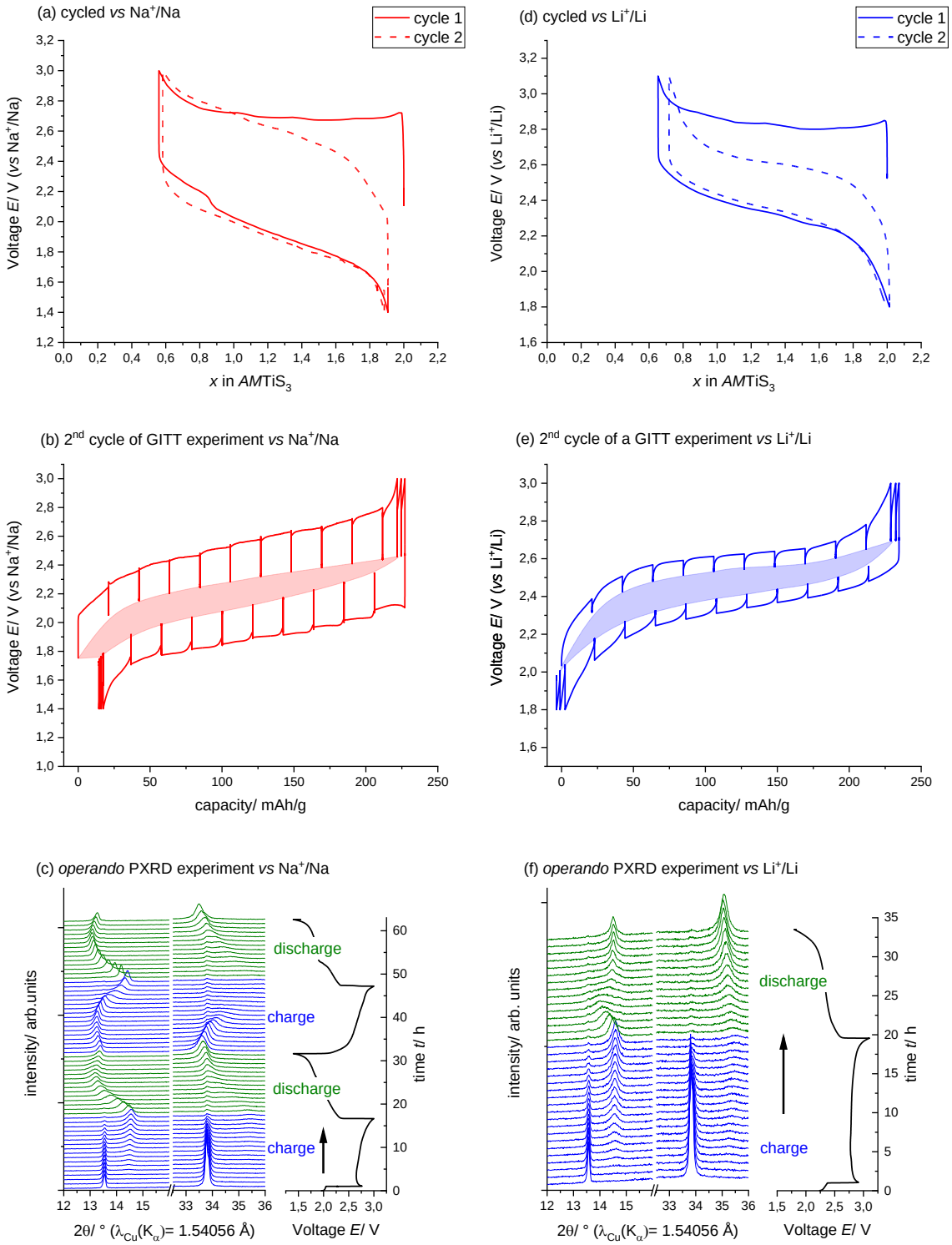


Figure S13: Electrochemistry of $Na_{1.5}[Li_{0.5}Ti]S_3$: Galvanostatic cycling, 2nd cycle of a GITT experiment and operando PXRD experiment vs Na^+/Na (a)-(c) and vs Li^+/Li (d)-(f) respectively.

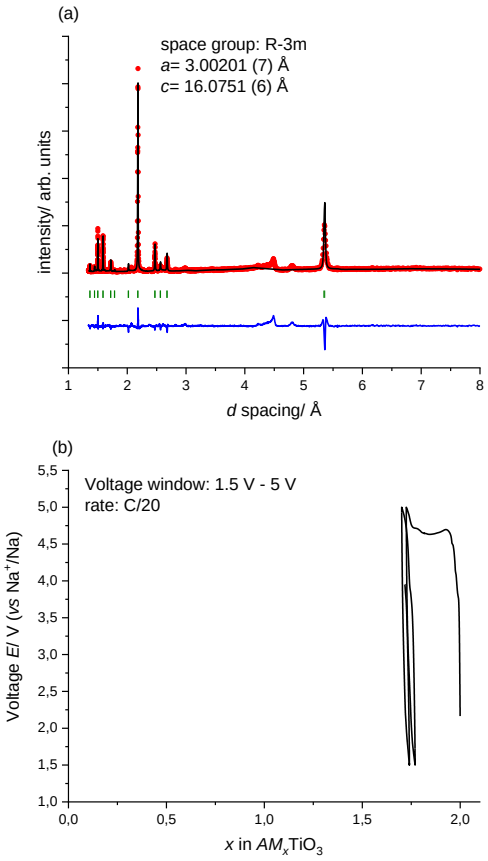


Figure S14: O3 type $Na_{1.5}[Li_{0.5}Ti]O_3$. (a) Pawley fit of $Na_{1.5}[Li_{0.5}Ti]O_3$ with the $R\bar{3}m$ space group. (b) Electrochemical cycling of $Na_{1.5}[Li_{0.5}Ti]O_3$ against Na^+/Na.

Tables

Table S1: Crystallographic data of Na_2TiS_3 as obtained from a combined NPD and SXRD Rietveld refinement at 300 K in the $C2/m$ space group (a= 6.43018(4) Å, b= 11.16335(7) Å, c= 6.89242(4) Å, β= 108.5878(4)°), χ^2(NPD): 5.58, χ^2(SXRD): 224.1.

Atom	Wyckoff site	*x/a*	*y/b*	*z/c*	U_{iso}/ Å^2	occupancy
S1	4*i*	0.2033(4)	0	0.2114(4)	0.0173(6)	1
S2	8*j*	0.2555(3)	0.31668(14)	0.2121(2)	0.0184(4)	1
Ti1	4*g*	0	0.16821(15)	0	0.0174(5)	0.903(4)
Na1	4*g*	0	0.16821(15)	0	0.0174(5)	0.097(4)
Ti2	2*b*	0	0.5	0	0.0180(13)	0.194(8)
Na2	2*b*	0	0.5	0	0.0180(13)	0.806(8)
Na3	2*c*	0	0	0.5	0.0238(14)	1
Na4	4*h*	0	0.3432(3)	0.5	0.0237(9)	1

Table S2: Crystallographic data of Na_2ZrS_3 as obtained from SXRD Rietveld refinement in the $C2/m$ space group (a= 6.65067(2) Å, b= 11.52461(4) Å, c= 6.95383(2) Å, β= 108.7912(2)°), χ^2(SXRD): 9.9.

Atom	Wyckoff site	*x/a*	*y/b*	*z/c*	U_{iso}/ Å^2	occupancy
S1	4*i*	0.2335(4)	0	0.2229(3)	0.0140(8)	1
S2	8*j*	0.2491(3)	0.32494(18)	0.2223(2)	0.0190(5)	1
Zr1	4*g*	0	0.16803(10)	0	0.021281(13)	0.904480(4)
Na1	4*g*	0	0.16803(10)	0	0.021281(13)	0.095520(4)
Zr2	2*b*	0	0.5	0	0.01656(4)	0.191041(8)
Na2	2*b*	0	0.5	0	0.01656(4)	0.808959(8)
Na3	2*c*	0	0	0.5	0.0201(15)	1
Na4	4*h*	0	0.3323(4)	0.5	0.0313(10)	1

Table S3: Crystallographic data of Na_2TiSe_3 as obtained from SXRD Rietveld refinement in the $C2/m$ space group (a= 6.747421(17) Å, b= 11.72281(3) Å, c= 7.219521(17) Å, β= 108.59178(16)°), χ^2(SXRD): 10.1.

Atom	Wyckoff site	*x/a*	*y/b*	*z/c*	U_{iso}/ Å^2	occupancy
Se1	4*i*	0.20673(18)	0	0.21195(18)	0.0214(3)	1
Se2	8*j*	0.25541(13)	0.31708(6)	0.21511(11)	0.0230(2)	1
Ti1	4*g*	0	0.16881(19)	0	0.0217(6)	0.87508(6)
Na1	4*g*	0	0.16881(19)	0	0.0217(6)	0.12492(6)
Ti2	2*b*	0	0.5	0	0.0292(15)	0.24984(12)
Na2	2*b*	0	0.5	0	0.0292(15)	0.75016(12)
Na3	2*c*	0	0	0.5	0.0251(18)	1
Na4	4*h*	0	0.3430(4)	0.5	0.0318(12)	1

Table S4: Crystallographic data of Na_2ZrSe_3 as obtained from SXRD Rietveld refinement in the $C2/m$ space group (a= 6.9425(5) Å, b= 12.0342(9) Å, c= 7.2685(5) Å, β= 108.74088(19)°), χ^2(SXRD): 9.4.

Atom	Wyckoff site	*x/a*	*y/b*	*z/c*	U_{iso}/ Å^2	occupancy
Se1	4*i*	0.2206(2)	0	0.2228(2)	0.0190(4)	1
Se2	8*j*	0.25256(16)	0.32289(7)	0.22372(12)	0.0140(2)	1
Zr1	4*g*	0	0.16799(12)	0	0.021276(15)	0.8854(17)
Na1	4*g*	0	0.16799(12)	0	0.021276(15)	0.1146(17)
Zr2	2*b*	0	0.5	0	0.014020(7)	0.229(3)
Na2	2*b*	0	0.5	0	0.014020(7)	0.771(3)
Na3	2*c*	0	0	0.5	0.022(2)	1
Na4	4*h*	0	0.3385(5)	0.5	0.0319(15)	1

Table S5 : Crystallographic data of the Rietveld refinement of electrochemically discharged Na_2TiS_3 in the $R\bar{3}m$ space group (a= 3.70249(7) Å, c= 19.8925(4) Å), χ^2(SXRD): 16.7.

Atom	Wyckoff site	*x/a*	*y/b*	*z/c*	U_{iso}/ Å^2	occupancy
S1	6*c*	0	0	0.25872(7)	0.1081(19)	1
Ti1	3*a*	0	0	0	0.1107(18)	2/3
Na1	3*a*	0	0	0	0.1107(18)	1/3
Na2	3*b*	0	0	0	0.074(2)	1

Table S6: Crystallographic data of $Na_{1.5}[Li_{0.5}Ti]S_3$ as obtained from a combined NPD and SXRD Rietveld refinement at 300 K in the $C2/m$ space group (a= 6.306851(17) Å, b= 10.93529(3) Å, c= 6.853729(15) Å, β=107.9597(2)°), χ^2(NPD): 6.5, χ^2(SXRD): 9.1.

Atom	Wyckoff site	*x/a*	*y/b*	*z/c*	U_{iso}/ Å^2	occupancy
S1	4*i*	0.2175(3)	0	0.2077(2)	0.0135(5)	1
S2	8*j*	0.2466(2)	0.32346(12)	0.21081(14)	0.0129(3)	1
Ti1	4*g*	0	0.16819(13)	0	0.0159(3)	0.9107(13)
Li1	4*g*	0	0.16819(13)	0	0.0159(3)	0.0893(13)
Ti2	2*b*	0	0.5	0	0.029(2)	0.179(3)
Li2	2*b*	0	0.5	0	0.029(2)	0.821(3)
Na3	2*c*	0	0	0.5	0.0194(10)	1
Na4	4*h*	0	0.3374(2)	0.5	0.0220(6)	1

Table S7: Overview of phases present in upscale batch of $N_{1.5}[Li_{0.5}Ti]S_3$.

Material	Detection method	Weight percent
$Na_{1.5}[Li_{0.5}Ti]S_3$	SXRD	> 94%
TiO_2 (Anatase)	SXRD	< 1%
TiO_2 (Rutile)	SXRD	< 1%
$Na_5Li_3Ti_2S_8$	SXRD	~ 4%

Experimental NMR fits (Figure 8a,b in main text)

The spectrum of pristine Na_2TiS_3, processed with an exponential apodization (line broadening of 50 Hz), was fitted in Dmfit ,[1] after a spline correction of the baseline, using the INT2QUAD model. The starting parameters if the fit were obtained by fitting a z-filtered MQMAS experiment.[2] Two sites are detected; the first has a relatively symmetric environment (C_Q=750 kHz), the latter has a more distorted environment (C_Q=1750 kHz). A careful integration of the central transition provides an average of 1:3 between the two signals. Based on the integration, we assume that Na#1 corresponds to the Na(1) in the Ti layers while the Na3 and Na4 sites in the Na layers are in exchange, thus resulting in the Na#2 peak.

Table S8: NMR parameters obtained by fitting the ^{23}Na NMR spectrum of Na_2TiS_3. The chemical shift and quadrupolar tensors are aligned.

	Gaussian Broadening (ppm)	Chemical shift			Quadrupolar interaction		Integration of central transition
Na site		Isotropic shift (ppm) δ_{CS}	Anisotropy (ppm) $\Delta\delta_{CS}$	η_{CS}	Quadrupole coupling constant (kHz) C_Q	η_Q	
#1	2.9	9.9	0	0	750	0	25% (0.5 Na)
#2	7.0	12.4	0	0	1800	1	75% (1.5 Na)

The same approach was applied to the ^{23}Na NMR spectrum of pristine $Na_{1.5}Li_{0.5}TiS_3$ recorded at 4.7 T. exponential apodization, spline correction of the baseline and starting parameters from a dedicated z-filtered MQ-MAS were used to fit the spectrum in Dmfit. This time the assignment is ambiguous, as 0.5 Li replaced 0.5 Na. The two environments are broader, most probably due to expected enhanced disorder in that phase.

Table S9: NMR parameters obtained by fitting the ^{23}Na NMR spectrum of $Na_{1.5}Li_{0.5}TiS_3$. The chemical shift and quadrupolar tensors are aligned.

	Gaussian Broadening (ppm)	Chemical shift			Quadrupolar interaction		Integration of central transition
Na site		Isotropic shift (ppm) δ_{CS}	Anisotropy (ppm) $\Delta\delta_{CS}$	η_{CS}	Quadrupole coupling constant (kHz) C_Q	η_Q	
#1	3.6	8.0	0	0	1480	0.6	55% (0.8 Na)
#2	17.0	9.0	0	0	2260	0.1	45% (0.7 Na)

CASTEP calculations to confirm assignments (Figure 8c,d)

In order to confirm these assignments and the uncertainties on each, DFT calculations were performed using the CASTEP 20 software[3] with the PBE functional[4] and the on-the-fly pseudopotentials generated by CASTEP. Calculations were performed with a cut-off energy of 600eV and with a tolerance for the convergence of the self-consistent field of 10^{-7}eV. The number of k points was determined in order to have a maximum distance of 0.04A^{-1} between two k points. Input structures were created from CIF files by removing the partial substitutions and converted to CASTEP format using cif2cell program.[5]

Atom's positions of all the structures were optimized by keeping the symmetry operations with an energy's tolerance of $5*10^{-6}$eV, a force tolerance of 0.01eV/A, and a displacement tolerance of $5*10^{-4}$ A. The unit cell parameters were kept fixed at the experimentally determined values.

NMR parameters were calculated using the GIPAW method[6] implemented in CASTEP with the same parameters. In order to compare GIPAW results with experimental spectra in Figure S8 (main text), the spectra were simulated using the DMfit software.[1] The chemical shifts of all sites were referenced in order to match the experimental chemical shift (no prior calibration).

Table S10: NMR parameters for Na_2TiS_3 predicted using CASTEP

	Guassian Broadening (ppm)	Chemical shift			Quadrupolar interaction		Multiplicity
Na site		Isotropic (ppm) δ_{CS}	Anisotropy (ppm) $\Delta\delta_{CS}$	Asymmetry η_{CS}	Quadrupole coupling constant (kHz) C_Q	Assymetry η_Q	
Na2 (Ti layers)	5.3	9.9	-5.5	0.6	695	0.1	0.5 Na
Na3	5.8	11.6	2.6	0.2	3130	0.2	1 Na
Na4	6.6	13.8	4.5	0.4	1820	0.8	0.5 Na

The calculation on Na_2TiS_3 is in relatively good agreement with the experimental data. Na3 is very broad in the static structure. Based on the intensities we hypothesize that we detect all the signals hence Na3 is most probably on exchange with Na4, which results in a smaller quadrupolar effect.

We turn to $Na_{1.5}Li_{0.5}TiS_3$ to better understand the experimental results. The CASTEP prediction of the shifts is given in Table S4. The partial substitution of Ti by the alkali atoms was removed to simplify the calculation. Two broad signals are predicted, in relatively good agreement with the experimental spectrum, especially if one assumes that the quadrupolar effect is lowered by mobility. This comforts the hypothesis of a layered material with Li in the Ti layers and Na in the S layers.

Table S11: NMR parameters for $Na_{1.5}Li_{0.5}TiS_3$ predicted using CASTEP.

	Broadening	Chemical shift			Quadrupolar interaction		Multiplicity
Na site		Isotropic (ppm) δ_{CS}	Anisotropy (ppm) $\Delta\delta_{CS}$	Asymmetry η_{CS}	Quadrupolar constant (kHz) C_Q	Assymetry η_Q	
Na3	3.8	2.7	4.2	0.7	1335	0.1	1 Na
Na4	11.3	3.8	10.1	0.6	2150	0.0	0.5 Na

References

(1) Massiot, D.; Fayon, F.; Capron, M.; King, I.; Le Calvé, S.; Alonso, B.; Durand, J.-O.; Bujoli, B.; Gan, Z.; Hoatson, G. Modelling One- and Two-Dimensional Solid-State NMR Spectra. *Magn. Reson. Chem.* **2002**, *40* (1), 70–76. https://doi.org/https://doi.org/10.1002/mrc.984.

(2) Amoureux, J. P.; Fernandez, C.; Steuernagel, S. Z Filtering in MQMAS NMR. *J. Magn. Reson. Ser. A* **1996**, *123* (1), 116–118. https://doi.org/DOI 10.1006/jmra.1996.0221.

(3) Pickard, C. J.; Mauri, F. All-Electron Magnetic Response with Pseudopotentials: NMR Chemical Shifts. *Phys. Rev. B* **2001**, *63* (24), 245101.

(4) Perdew, J. P.; Burke, K.; Ernzerhof, M. Generalized Gradient Approximation Made Simple. *Phys. Rev. Lett.* **1996**, *77* (18), 3865–3868. https://doi.org/DOI 10.1103/PhysRevLett.77.3865.

(5) Björkman, T. CIF2Cell: Generating Geometries for Electronic Structure Programs. *Comput. Phys. Commun.* **2011**, *182* (5), 1183–1186.

(6) Yates, J. R.; Pickard, C. J.; Mauri, F. Calculation of NMR Chemical Shifts for Extended Systems Using Ultrasoft Pseudopotentials. *Phys. Rev. B* **2007**, *76* (2), 24401.